AFOSR 69-1458TR

PRODUCTION OF HIGH CURRENT DENSITY ION BEAMS BY ELECTROHYDRO DYNAMIC SPRAYING TECHNIQUES

by
DONALD S. SWATIK

14 MAY 1969

CHARGED PARTICLE RESEARCH LABORATORY
REPORT NO. CPRL-3-69
DEPARTMENT OF ELECTRICAL ENGINEERING
ENGINEERING EXPERIMENT STATION
UNIVERSITY OF ILLINOIS
URBANA, ILLINOIS

PRODUCTION OF HIGH CURRENT DENSITY ION BEAMS BY ELECTROHYDRODYNAMIC SPRAYING TECHNIQUES

by

DONALD STEPHEN SWATIK

14 MAY 1969

Supported by

Air Force Office of Scientific Research

CHARGED PARTICLE RESEARCH LABORATORY
REPORT NO. CPRL-3-69
DEPARTMENT OF ELECTRICAL ENGINEERING
ENGINEERING EXPERIMENT STATION
UNIVERSITY OF ILLINOIS
URBANA, ILLINOIS

ABSTRACT

The production of high current density ion beams by the direct interaction of an intense electric field on a liquid surface was investigated. Electrohydrodynamic spraying techniques, which have been traditionally utilized for the production of multi-molecular charged particle beams, were optimized for the production of ionic particles.

Simultaneous ion formation and acceleration was achieved by applying a high DC voltage between a hemispherical liquid meniscus supported at the tip of a metallic capillary and a concentric, planer accelerating electrode. With proper feed-back control of the applied voltage and proper wetting of the capillary by the working fluid the hemispherical meniscus could be deformed by the action of the applied electric field into a stable conical geometry. At the apex of this cone the electric field intensity was of sufficient amplitude to field evaporate ions from the liquid surface. Such a field evaporation source using a liquid anode can operate indefinitely at high emitted current levels.

The field evaporated particles were analyzed to determine the usefulness of this technique as a source of charged particles for electrostatic microthrusters. The total emitted current, specific charge distribution of the emitted particle, and formation energy of the particles were measured in terms of the operating parameters of the system.

Stable ion currents of up to 500 microamps were obtained from a single capillary emitter. The ion beam consisted of 75% gallium dimers, 24% indium dimers and 1% gallium tetramers. The resulting thrust produced was 73.8 micronewtons.

ACKNOWLEDGMENT

I would like to take this opportunity to thank my thesis adviser Professor Charles D. Hendricks, Jr., for his advice and guidance that contributed greatly to the ultimate writing of this dissertation.

In addition, I would like to express my appreciation to the entire staff of the Charged Particle Research Laboratory for their many helpful comments and criticisms of my work. Special thanks is extended to Mrs. Dona Baucom for her able assistance in the preparation of the manuscript.

Finally, I would like to thank my parents, Mr. and Mrs. Stephen Swatik, Jr., for making my college education possible and for their unfaltering encouragement and enthusiasm throughout my college career.

This work was supported by the Air Force Office of Scientific Research under grant AFOSR 68-1508 and by a NDEA Title IV predoctoral fellowship.

TABLE OF CONTENTS

LIST OF SYMBOLS

Symbol	Description
A	Mass number
a	(1) Radius
	(2) Normalized quadrupole DC voltage
a_o	Radius at apex of cone
a_1	Interelectrode spacing
a_r	Unit vector in r direction
a_θ	Unit vector in θ direction
a_x	Unit vector in x direction
a_y	Unit vector in y direction
e	Electronic charge
F	Force
F(E)	Energy distribution function
F_k	Velocity density function
f	Frequency
f(v)	Velocity distribution function
g	Normalizing radius
I	Current
I_n	nth ionization potential
$i(t_d)$	Current probability density as a function of drift time
$i(q_s)$	Current probability density as a function of specific charge
J	Current density

Symbol	Description
K	Curvature
k	Boltzmann constant
L	Drift space length
M_e	Final mass
M_l	Payload mass
M_o	Initial mass
M_p	Propellant mass
M_w	Power plant mass
m	Mass
m_1	Particle mass
m_2	Particle mass
$\dot{m}$	Mass flow rate
N	Number of lattice sites
n	(1) Mode of instability
	(2) Order of Legendre Polynomial
	(3) Number of elementary charge on an ion
P	Kinetic power
$P_n(\cos\theta)$	Legendre polynomial of order n and argument $(\cos\theta)$
p	Radius of curvature
p_o	Radius of curvature at apex of cone
p_1	A principle radius of curvature
p_2	A principle radius of curvature
Q	Depth of potential well
Q_o	Depth of zero-field potential well

Symbol	Description
q	(1) Charge
	(2) Normalized quadrupole AC voltage
q_s	Specific charge
R	(1) Resistance
	(2) Normalized radius
r	Radial coordinate
r_o	Quadrupole geometric constant
r_1	Minimum radius of cone
r_2	Maximum radius of cone
T	Temperature
t	Time
t_o	Propulsion time
$U_I(x)$	Ionic potential energy
u	Terminal velocity
V	Voltage
V_a	Accelerating voltage
V_{ac}	Quadrupole AC voltage
V_B	Space charge potential
V_c	Potential at center of ion beam
V_{dc}	Quadrupole DC voltage
V_f	Formation potential
V_o	Applied voltage
V_R	Retarding potential
$V(t)$	Time varying voltage
V_z	Ohmic potential drop

Symbol	Description
v	Velocity
$\bar{v}$	Average velocity
W	Normalized potential
W_L	Formation energy
X	Energy ratio
x	Rectangular coordinate
x_c	Intersection distance
y	Rectangular coordinate
α	(1) Specific power
	(2) Semi-vertical angle of cone
Γ	Stress due to surface tension
γ	Surface tension
$\mathcal{E}$	Electric field intensity
e_o	Capacitivity of free space
η_b	Beam conversion efficiency
η_f	Formation efficiency
θ	(1) Angular coordinate
	(2) Normalized quadrupole frequency
Λ	Sublimation energy
ρ	(1) Resistivity
	(2) Volume charge density
Σ	Summation
τ	Evaporation time constant
τ_o	Reciprocal Einstein frequency

Symbol	Description
ϕ	Potential
ϕ_o	Electronic work function
ω	Angular frequency

LIST OF FIGURES

Figure Page

1. ELECTROSTATIC PROPULSION

1.1 Motivation

Ever since Tsiolkovskii(1) wrote his now famous rocket equation that relates the terminal velocity of a space vehicle to its exhaust velocity and mass ratio, rocket designers have recognized the need for a thrustor with a high exhaust velocity and low propellant mass flow rate. The exhaust velocity of a chemical rocket is limited by the enthalpy of the reaction between the fuel and oxidizer. The most energetic propellant combinations such as hydrogen-oxygen and hydrogen-fluorine do not yield sufficiently high exhaust velocities for optimum payload ratios or terminal velocities. Consequently, a new source of thrust was needed that would operate more efficiently than chemical systems.

The use of electrostatically accelerated ions to produce thrust was suggested by Goddard in 1906.(2) An electrostatic thrustor represents, at least ideally, a highly efficient means of converting stored energy into thrust. The thrust produced is usually very small compared to that of chemical rockets, and for this reason electrically propelled vehicles cannot operate under conditions where appreciable atmospheric drag is encountered or where the trajectory demands propulsion against large gravity forces. Electric thrustors function by applying a small thrust for a very long period of time, whereas chemical rockets produce a very large thrust for a short time. For many missions planned for the near future, electric propulsion systems show marked advantages in overall operational efficiency over chemical rockets.(3)

It has been the intent of this research to further the state-of-the-art of electrostatic propulsion systems. In the following section the physics of electrostatic thrustors will be outlined and the important criteria of a beam of charged particles used for thrust production will be discussed. On the basis of these criteria, existing electrostatic propulsion systems will be explained and compared. Finally, noting the operation of current electrostatic thrustors and the design parameters imposed by the physical laws governing the motion of space vehicles, the objectives of this study will be put forth.

1.2 Physics of Electrostatic Thrustors

A. Electrostatic Acceleration

The motion of a space vehicle is governed by Newton's laws. An isolated space vehicle can be accelerated by emitting a propellant of mass m with an exhaust velocity v. The force which expels the propellant particles is equal to the rate of change of momentum of the propellant which is given by Newton's second law.

$$F = \frac{d(mv)}{dt} \qquad (1\text{-}1)$$

For electrostatic systems the exhaust velocity v is constant and is determined by the accelerating voltage V_a and the specific charge of the propellant particles q_s through the relationship

$$v^2 = 2V_a q_s \qquad (1\text{-}2)$$

The exhaust velocity is plotted as a function of the accelerating voltage for various particle specific charges in Fig. (1-1).

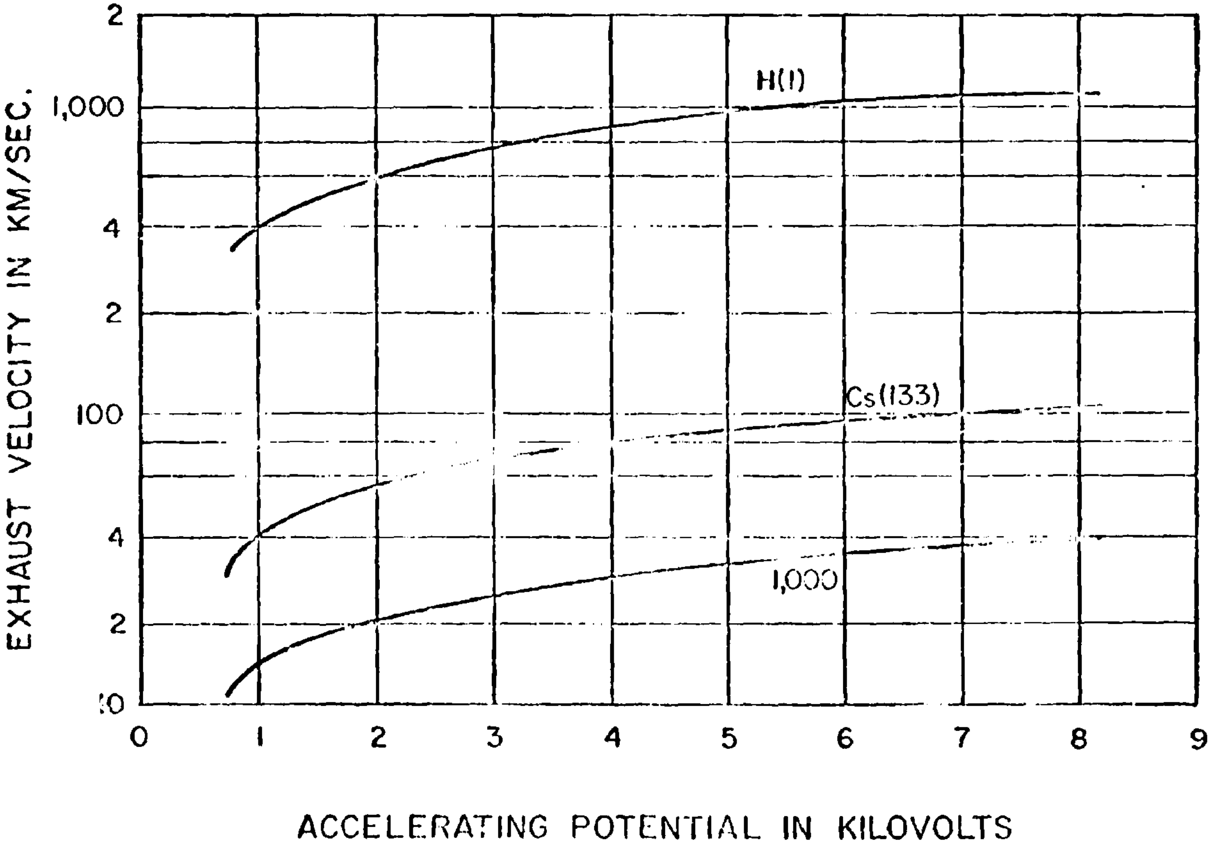

FIG. 1-1 EXHAUST VELOCITY AS A FUNCTION OF ACCELERATING POTENTIAL WITH PARTICLE SPECIFIC CHARGE AS A PARAMETER

For a constant exhaust velocity system Newton's second law takes the form

$$F = \dot{m}v \qquad (1\text{-}3)$$

where $\dot{m}$ is the time rate of change of propellant mass or mass flow rate. The same force F that expels the propellant also acts upon the vehicle as expressed by Newton's third law.

The thrust can be written in terms of the total emitted current, I, and accelerating voltage as

$$F = I\left(\frac{2V_a}{q_s}\right)^{1/2} \qquad (1\text{-}4)$$

The thrust produced is directly proportional to the emitted particle current and inversely proportional to the specific charge. Hence, to attain a large thrust either the emitted current must be large or the particle specific charge small or both.

B. Power Conversion Efficiency

An electrostatic thrustor functions by converting electrical energy into thrust. The efficiency of this conversion process can be divided into two components. The first concerns the transformation of electrical energy into beam kinetic energy, and the second the relationship between this kinetic energy and the thrust produced.

The formation efficiency of an electrostatic thrustor is expressed in terms of the kinetic energy given to a particle, qV_a, and the energy, W_L, which is lost in forming the particle.

$$\eta_f = \frac{qV_a}{qV_a + W_L} \qquad (1\text{-}5)$$

The formation energy consists of the energy needed to evaporate the propellant, control the propellant flow, support the ionization itself, supply heat lost through conduction and radiation, ohmic losses, and space charge effects. The formation efficiency is plotted as a function of the accelerating voltage in Fig. (1-2). In order to maintain a high formation efficiency either the energy loss per particle must be low or the accelerating voltage high or both.

The thrust producing capability of a charged particle beam with a specified kinetic energy is given by its beam conversion efficiency. The kinetic power of the beam is given by

$$P = 1/2\ \dot{m}v^2 \qquad (1\text{-}6)$$

By dividing Eqn. (1-3) by (1-6) the thrust per unit power is obtained

$$\frac{F}{P} = \frac{\dot{m}v}{1/2\ \dot{m}v^2} = \frac{2}{v} \qquad (1\text{-}7)$$

Most physical electrostatic thrustors do not expel all propellant particles at the same velocity. Instead the exhaust beams possess a velocity distribution. The effect of a velocity distribution is to reduce the thrust produced per unit of beam power.

If the system has a velocity distribution given by

$$f(v) = \sum F_k v_k \qquad (1\text{-}8)$$

where F_k is the fraction of particles possessing velocity v_k, then the thrust per unit power can be written as

$$\frac{F}{P} = \frac{2}{\sum F_k v_k} \frac{\left(\sum F_k v_k\right)^2}{\sum F_k v_k^{\ 2}} \qquad (1\text{-}9)$$

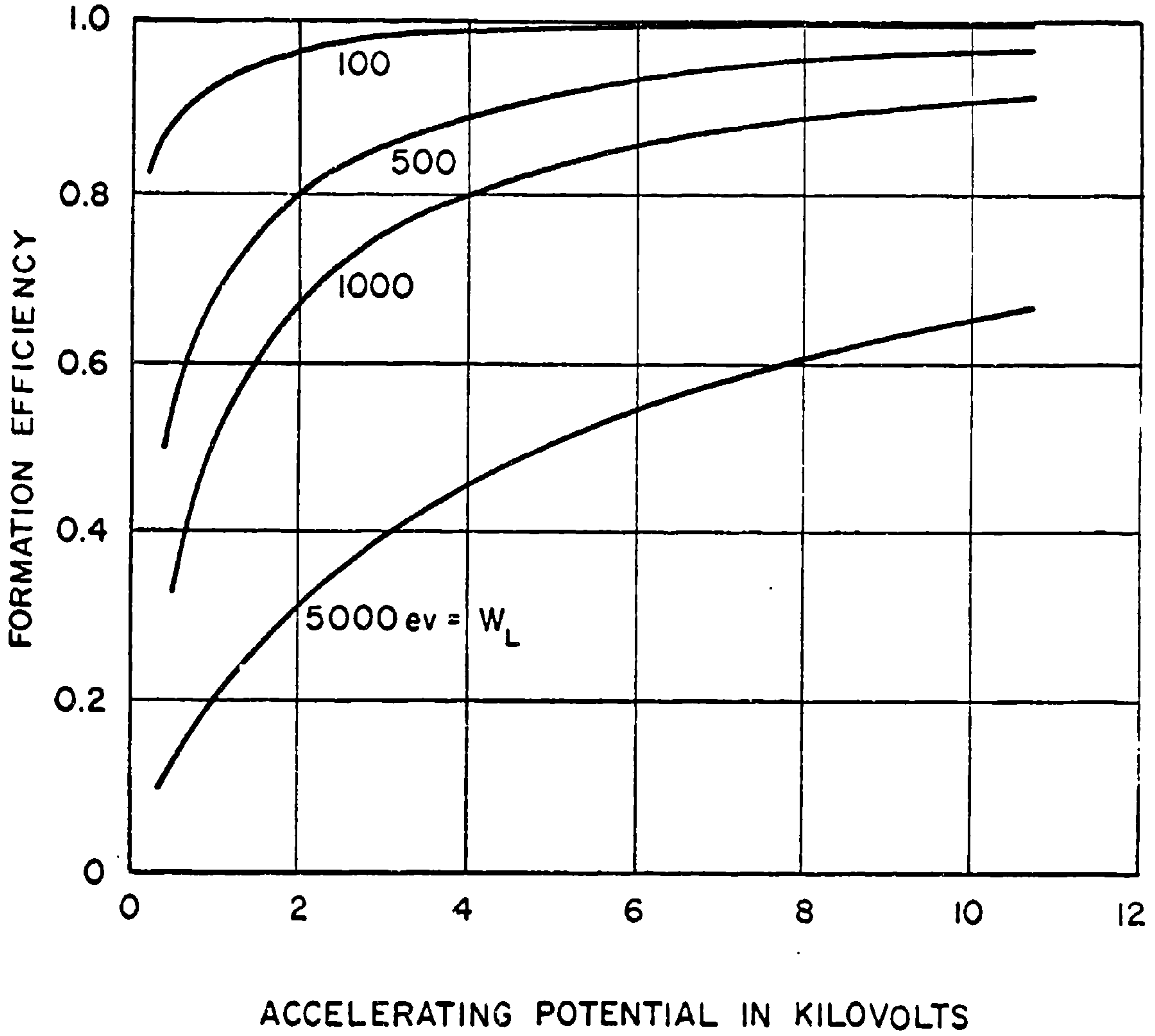

FIG. 1-2 FORMATION EFFICIENCY AS A FUNCTION OF ACCELERATING POTENTIAL WITH FORMATION ENERGY AS A PARAMETER

For a distribution containing only a single velocity, Eqn. (1-9) reduces to Eqn. (1-7), and the degradation in efficiency produced by a multi-velocity distribution, or beam conversion efficiency, is seen to be given by

$$\eta_b = \frac{\left(\sum F_k v_k\right)^2}{\sum F_k v_k^{\,2}} \qquad (1\text{-}10)$$

It immediately follows that the summations in the above equation can be replaced by statistical average values

$$\eta_b = \frac{\bar{v}^2}{\overline{v^2}} \qquad (1\text{-}11)$$

and finally, using Eqn. (1-2), the averaged velocities can be replaced with the corresponding averaged specific charges.

$$\eta_b = \frac{\left(\overline{q_s^{\,1/2}}\right)^2}{\overline{q_s}} \qquad (1\text{-}12)$$

Accordingly, in an electrostatic thrustor, the beam conversion efficiency is a function of the variance of the specific charge distribution of the expelled beam. A system with only one specific charge present produces the maximum thrust per unit of beam power; as the distribution broadens the efficiency is reduced. For a Maxwellian distribution, the beam conversion efficiency is approximately 85%.

C. Optimum Exhaust Velocity

The terminal velocity u of a space vehicle in a drag free, gravity free space is related to the exhaust velocity of its propellant v, and its total mass ratio M_e / M_o by Tsiolkovskii's equation.$^{(1)}$

$$u = v \ln (M_o/M_e) \tag{1-13}$$

where M_o, the total initial mass and M_e, the burnout or final mass are given by

$$\begin{aligned} M_o &= M_p + M_w + M_l \\ M_e &= M_w + M_l \end{aligned} \tag{1-14}$$

where M_p is the propellant mass, M_w the power plant mass, and M_l the payload mass.

By eliminating the power plant mass from Eqn. (1-13), the payload ratio M_l / M_o can be determined as a function of the exhaust velocity. The propellant flow rate $\dot{m}$, propulsion time t_o, and propellant mass M_p are related by

$$M_p = \dot{m} t_o \tag{1-15}$$

Hence, the beam kinetic power can be written as

$$P = \frac{\dot{m} v^2}{2} = \frac{M_p v^2}{2 t_o} \tag{1-16}$$

The beam power per unit of power plant mass is defined as the specific power α of the system

$$\alpha = \frac{P}{M_w} \tag{1-17}$$

By combining Eqns. (1-13) to (1-17) the payload ratio M_l / M_o is obtained as a function of the exhaust velocity.

$$\frac{M_l}{M_o} = \mathrm{EXP}(-u/v) - \frac{v^2}{2\alpha t_o} (1 - \mathrm{EXP}(-u/v)) \tag{1-18}$$

The payload ratio, unlike the total mass ratio, depends not only on the exhaust and terminal velocities, but also on the specific power and total propulsion time.

For a given terminal velocity, specific power, and propulsion time the payload ratio can be maximized as a function of the exhaust velocity. The location of the maximum is found by differentiating Eqn. (1-18) with respect to the exhaust velocity. The optimum exhaust velocity is given by

$$\frac{2\alpha t_o}{v^2} = \frac{2v}{u}\,(\mathrm{EXP}(u/v) - 1) - 1 \tag{1-19}$$

and the corresponding maximum payload ratio is

$$\frac{M_1}{M_o} = \frac{1 - (u/2v)(1 + v^2/2\alpha t_o)}{1 + (u/2v)(1 + 2\alpha t_o/v^2)} \tag{1-20}$$

Consequently, for a given terminal velocity the payload ratio can be maximized, likewise at a specified payload ratio the terminal velocity can be optimized. The payload ratio is plotted as a function of exhaust velocity with terminal velocity as a parameter in Fig. (1-3). All velocities were normalized by setting $2\alpha t_o = 1$.

1.3 Comparison of Electrostatic Propulsion Systems

In the previous section the physics of electrostatic energy conversion was outlined. Various parameters of a charged particle beam were deemed important to its overall performance as a means of converting electrical energy into thrust. First, the formation energy of a particle must be small compared to the kinetic energy it acquires; second, the variance of the particle specific charge distribution should be small; third, the

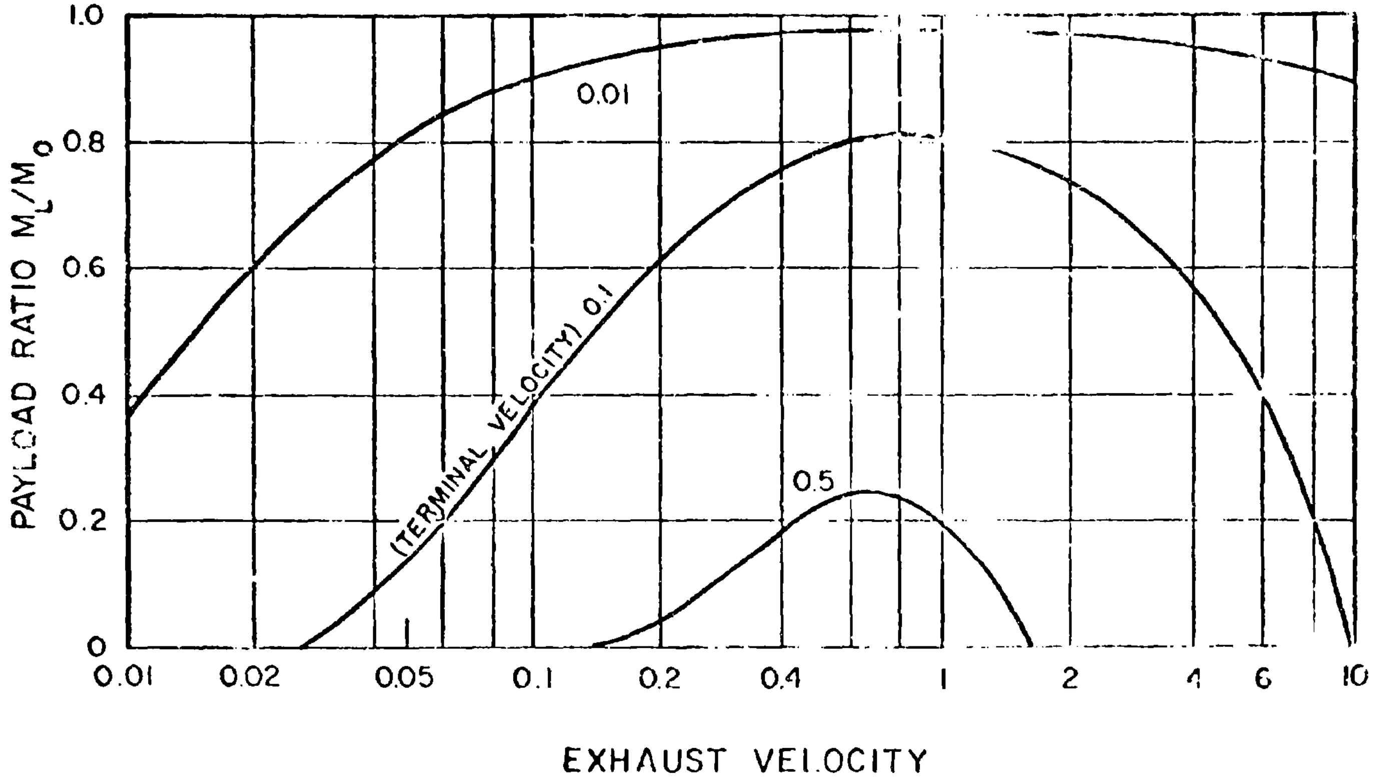

FIG. 1-3 PAYLOAD RATIO AS A FUNCTION OF EXHAUST VELOCITY WITH TERMINAL VELOCITY AS A PARAMETER

total emitted current should be large; and, fourth, the exhaust velocity should be optimized for either maximum payload ratio, or maximum terminal velocity or other mission parameter.

Electrostatic thrustors can be divided into two classes - ionic and heavy particle propellant. Each scheme will be discussed and the advantages and disadvantages of both systems will be compared using the four criteria listed above.

A. Ionic Propellant

Ionic propellant electrostatic thrustors function in two discrete steps. First an ion is produced by one of several known ionization techniques, and then it is accelerated to a given velocity by an electrostatic field. Many different methods of ionizing atoms have been developed since Rutherford(4) and Thomson(5) made the original studies on the conduction of electricity through gases. Langmuir(6) and Taylor(7) performed much of the original experimental and theoretical work on surface ion sources. In 1940, Finkelstein(8) examined the ionization of gases by high energy electrons and developed the powerful electron bombardment ion source. A third type of ion source known as the duoplasmatron utilizes a magnetic pinch effect to produce a very dense plasma; it was conceived by von Ardenne in 1957.(9)

The surface ionization source was the first of the above to be proposed for ion engines(10) and is still the most commonly used technique. Surface ion sources utilize the fact that a high work function metallic surface may present a potential well to the electrons of a low ionization potential atom. Ionization occurs when an atom strikes the metallic surface. This surface ionization proceeds in two discrete steps. First an atom approaching the surface is polarized by image forces between its nucleus and free electrons in the metal. It will adhere to the surface by this coulomb attraction as an atom. When the temperature of the substrate is hot enough the atom will evaporate. If the ionization energy of the evaporating atom is greater than the work function of the substrate, the atom will evaporate as a neutral; but, if the work function is greater than the ionization energy the electron is trapped by the substrate and the adsorbed atom evaporates as an ion. If the substrate temperature is below a critical value, the atoms will evaporate as neutrals and above that temperature they will evaporate as ions.

Much work has been spent recently on the investigation of the ionization properties of cesium on porous tungsten.(11) Cesium is the heaviest element that is useful in a surface ion source and thus is the most efficient for electric thrustors. Cesium on tungsten ion sources have a theoretical ionization efficiency of 99.5% and laboratory experiments have yielded efficiencies in this range. Hence, such a source produces over 99% ions and less than 1% neutral atoms, and the variance of the corresponding specific charge distribution is very low.

One of the main limitations of cesium systems is the energy loss per ion produced. Surface temperatures in the 1100 - 1500° K range are necessary for efficient ion production, and hence heat losses by conduction and radiation are large and may amount to more than 1000 ev per ion. Therefore, in order to obtain a high formation efficiency the accelerating voltage must be high, but this in turn produces a high exhaust velocity. Thus, for many missions, a cesium ion source cannot simultaneously attain a high formation efficiency and an optimum exhaust velocity.

B. Heavy Particle Propellant

The basic limitation in formation efficiency of ionic propellant systems can be overcome by using a heavy particle propellant. If the mass of the propellant particles is increased a higher accelerating potential can be used to attain a desired exhaust velocity. Hence, by varying the specific charge of the propellant, the two desirable conditions of a high accelerating potential and an optimum exhaust velocity can be achieved simultaneously.

The most widely used and most efficient method of producing heavy particles is by the electrohydrodynamic (EHD) spraying of liquids from electrified capillaries. By placing a small diameter capillary at a high potential (either positive or negative) relative to a nearby grounded electrode a high intensity electric field can be produced at the tip of the capillary. If a liquid is forced through the capillary it will form a hemispherical meniscus at the capillary tip and a surface charge will be induced on it by the electric field. If the outward stress of the surface charge is greater than the surface tension forces holding the meniscus together, it will disrupt and a spray of charged particles will be produced.

The EHD spraying of liquids has been investigated since 1745, when Bose(12) observed the formation of water threads at the tip of an electrified capillary. The physics of the spraying process was first formulated by Rayleigh in 1882(13) when he determined the stability criterion for a charged conducting droplet. Early experimenters believed that only low conductivity liquids could be electrically sprayed; hence, most experiments were performed with insulating liquids.(14) The charge and size of individual oil droplets electrically sprayed in a vacuum were measured by

Hendricks in 1959.(15)

In general, the EHD spraying of insulating liquids produced low emitted currents and broad specific charge distributions. Attempts to increase the emitted current were made by increasing the conductivity of the working fluid. Conducting liquids were first sprayed by Hendricks in 1960,(16) and liquid Wood's metal was sprayed by Krohn in 1961.(17) High currents were observed by both authors. Unfortunately, as higher currents were produced the propensity to produce ions increased. The resulting specific charge distributions contained both heavy particles and ions. Hence, the need arose for a more complete physical understanding of the spraying phenomenon.

In 1964, Hendricks(18) applied Rayleigh's theory to the case of a liquid hemisphere at a capillary tip and thus formally related the Rayleigh instability criterion to the physical spraying situation. A liquid hemisphere will become unstable when:

$$(2n + 1)\gamma = V_a^2/4\pi(300)^2 a \qquad (1\text{-}21)$$

where γ is the surface tension, a the radius and n the mode of the instability. The EHD spraying process was studied, using energy minimization techniques by Pfeifer in 1965(19) as a function of the applied electric field, $\mathcal{E}$, liquid mass flow rate and surface tension. For perfectly conducting liquids under the influence of high electric field intensities the following theoretical relationship for the specific charge of the emitted particles was obtained:

$$q_s = C_o \, \dot{m}^{-1/2}(\gamma \mathcal{E})^{1/2} \qquad (1\text{-}22)$$

where C_o is a constant of the working fluid.

On the basis of these theoretical studies and past research experience, studies of working fluids were undertaken in an attempt to optimize the production of heavy particles and eliminate the formation of ions. In general, the EHD spraying of non-conducting liquids has produced heavy particles in the size range useful for the electric propulsion systems. Unfortunately, these charged particle beams have only been produced at low current levels and with non-ideal specific charge distributions. Thus, by using heavy particles a high formation efficiency can be obtained, but only at the expense of a low emitted current and a less than 100% beam conversion efficiency.

1.4 Proposed Research

Heavy particle systems are capable of high formation efficiencies and ionic systems can produce high beam currents at high beam conversion efficiencies. Heavy particle systems were first introduced as a means of attaining a high formation efficiency by increasing the kinetic energy given to the propellant particles while maintaining a near optimum exhaust velocity. The more direct approach of decreasing the total energy expended in producing an ion has met with little success. Almost all of this energy loss in surface ionization systems can be attributed to heating effects in the entire system. If an ionization source could be devised that functions at low temperatures, the formation efficiency could be greatly increased.

One method of producing ions at room temperature is by the field evaporation of a surface. A sufficiently strong electric field applied to a metal surface in such a direction as to make the metal positive produces an emission of positive ions. Field evaporation was first observed by Müller in 1956(20) while experimenting with a field ion microscope (FIM). Field evaporation techniques have been utilized as a means of producing very smooth emitters for the FIM. Since any irregularities on the surface lead to locally high electric field intensities, they are preferentially evaporated and the end form is atomically smooth. By further increasing the applied electric field intensity the emitter can be disected a monolayer at a time and hence the "inside" of the emitter can be examined.(21)

If the field evaporated ions originate in an adsorbed layer or are produced by the emitter material itself, the ion source will be weak and rapidly exhausted. Müller has produced steady ion currents in the microampere range by supplying the ionizable matter in the gaseous phase.(22) The ionization of gaseous elements at an emitter held at a high potential is the basis of the FIM.

In 1967, Swatik(2[illegible] studied the EHD spraying of the eutectic alloy of gallium and indium and observed that under the appropriate operating conditions a beam consisting totally of ions could be produced by field evaporation of the working fluid. Thus, it was shown for the first time that an EHD spraying system could be optimized, not for the production of heavy particles, but for the production of ions! In such a system, the ionizable matter supplied in the liquid phase and the source can be operated indefinitely at high current levels because the evaporated mass can be constantly replenished.

Thus, it has been the goal of this research to further study the field evaporation of liquids by EHD spraying techniques. Ideally such a source of charged particles would have a very low energy loss per particle produced, a very narrow specific charge distribution, and a high beam current. Hence, it would possess the advantages of both heavy particle and ionic propellant systems and would represent a highly efficient means of converting electrical energy into thrust.

The working fluid used for field evaporation experiments must possess a low vapor pressure to retard evaporation in low pressure environments; a high surface tension to maintain stability against the action of the applied electric field; and a high conductivity to allow for the production of high currents. The eutectic alloy of 76% gallium and 24% indium was chosen as the working fluid for this study on the basis of its physical parameters. The melting point of the alloy is 15.7° C.(24) It is thus a liquid at room temperature. The alloy possesses a vapor pressure of less than 10^{-8} torr at room temperature.(25) The surface tension and conductivity of the alloy were measured by Zrnic and Swatik(26) and are 628 dynes/cm and 3.4×10^4 mho/cm respectively.

The first phase of this research was concerned with the production of a stable ion emission from the gallium-indium alloy. The design of the capillary and accelerating electrode will be analyzed; the regulation of the accelerating potential will be determined for optimum performance, and the stability of the liquid meniscus will be examined.

The second phase was the analysis of the particle beam with respect to its performance as an electrostatic thrustor. The parameters to be measured included the emitted current as a function of the applied electric field, the specific charge distribution as a function of the current, and the energy loss per particle as a function of the current.

2. FIELD EVAPORATION OF LIQUIDS

The mechanisms involved in the production of ions from an electrified liquid surface will be discussed in this chapter: (1) The shape which the liquid meniscus should take under the influence of surface tension and the applied electric field will be determined; (2) An approximate solution of Laplace's equation near the emitting surface will be formulated; (3) A theory explaining field evaporation will be derived from basic principles; and, (4) Several possible loss mechanisms in the beam formation process will be proposed.

2.1 Shape of the Meniscus

The action of electric fields on liquid surfaces has been theoretically studied since Rayleigh(13) derived a mathematical stability criterion for electrified, conducting, liquid spheres in terms of perturbations on their surfaces. This theory explained the incipient instability of a drop for infinitesimal deformation but did not predict or explain large deformations. In 1964, Taylor studied the "Disintegration of Water Drops in an Electric Field"(27) and found that a conical surface could exist in equilibrium under the influence of surface tension and an electric stress, and thus approached the problem of large scale deformations.

The inward stress due to surface tension at a point on a liquid surface is given by

$$\Gamma = \gamma\left(\frac{1}{p_1} + \frac{1}{p_2}\right) \tag{2-1}$$

where γ is the surface tension constant of the liquid and p_1 and p_2 are the two principle radii of curvature at the point in question.

For a conical surface one of the two radii is infinite at all points, and Eqn. (2-1) becomes

$$\Gamma = \frac{\gamma}{p_1} \tag{2-2}$$

It is evident that the curvature of a conical surface in spherical coordinates is inversely proportional to the radial coordinate r. The restoring stress of surface tension is then also inversely proportional to r, and an outward stress normal to the surface that can be in equilibrium with the surface tension must also be inversely proportional to r.

The stress of an electric field normal to a surface is a function of the second power of the field intensity. This implies that the potential must vary as $r^{1/2}$ so that the square of its gradient will vary as r^{-1}.

In spherical coordinates, a solution to Laplace's equation for the region bounded by a conducting conical surface and one of its equipotentials is given by

$$\phi = \sum \left[A_n + B_n \; r^r P_n(\cos\theta)\right] \tag{2-3}$$

where P_n $(\cos\theta)$ is the Legendre function of order n. This geometry is shown in Fig. (2-1a).

The electric field that is required for the equilibrium of the conical surface is then defined by the potential

$$\phi = V_o + B \, r^{1/2} P_{1/2}(\cos\theta) \tag{2-4}$$

where V_o is the voltage applied between the conical surface and the equipotential.

If $\theta = \theta_o$ is the conical equipotential surface where $V = V_o$, then

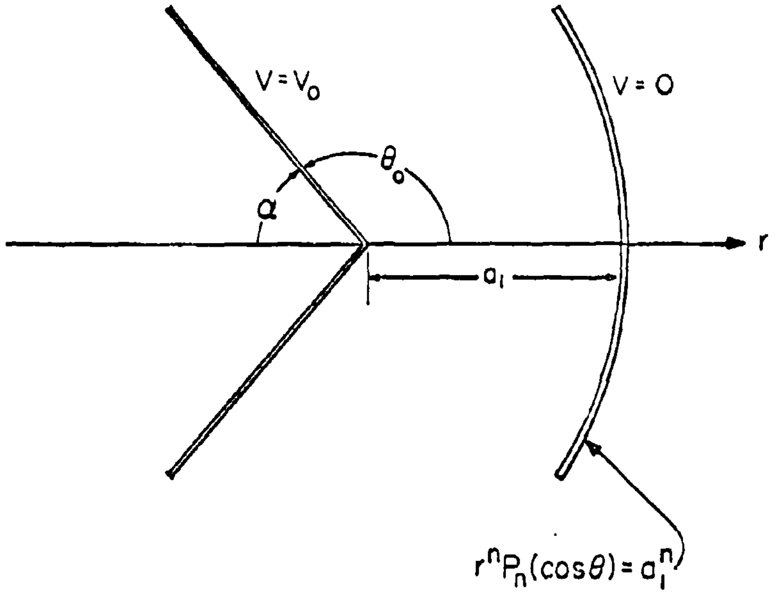

(a) CONICAL ANODE

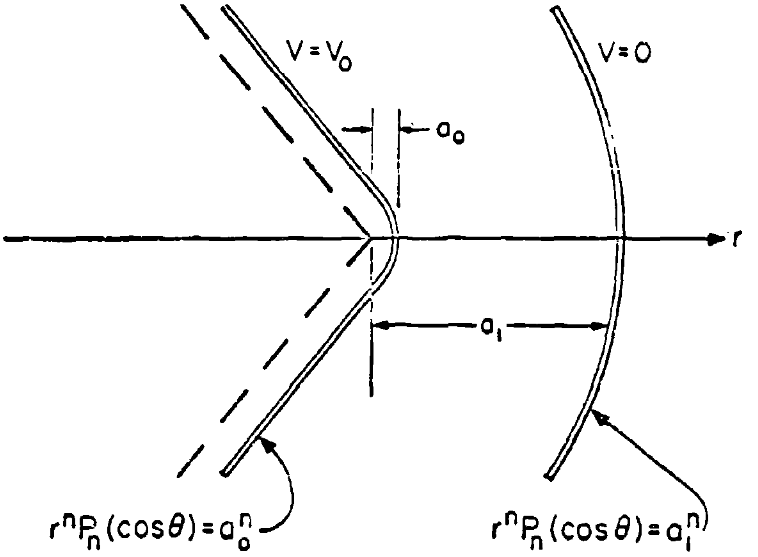

(b) MODIFIED ANODE

FIG. 2-1 CONICAL FIELD GEOMETRY

the Lengendre function must vanish at all points on the surface

$$P_{1/2}(\cos\theta) = 0 \qquad (2\text{-}5)$$

The function $P_{1/2}(\cos\theta)$ has only one zero in the range $0 < \theta < \pi$ at $\theta = 130.7^{\circ}$; hence, a conical surface can exist in equilibrium under the influence of an electric field if it has a vertical angle of 98.6°.

2.2 Electric Field Calculations for Conical Meniscus

After having determined that a conical geometry can be a stable configuration, it is necessary to analytically determine the electric field normal to the surface. The electric field is found by taking the negative gradient of the potential solution given in Eqn. (2-4) and applying the appropriate boundary conditions

$$\mathcal{E} = \frac{V_o}{a_1^{1/2}} \left[P_{1/2}(\cos\theta)\,\frac{0.5}{r^{1/2}}\,\hat{a}_r - \frac{\sin\theta}{r^{1/2}}\,\frac{\partial(P_{1/2}(\cos\theta))}{\partial(\cos\theta)} \right] \hat{a}_\theta \qquad (2\text{-}6)$$

where a_1 is the interelectrode spacing at $\theta = 0$, and $\hat{a}_r$ and $\hat{a}_\theta$ are unit vectors in the r and θ directions respectively. At $r = 0$ this solution gives an infinite electric field intensity. This is not physically realizable. To make the problem realistic, the conical surface can be replaced by one of the equipotential surfaces very near to it, defined by

$$r = a_o(P_{1/2}(\cos\theta))^{-2} \qquad (2\text{-}7)$$

where $a_o << a_1$. The equipotential approximation is shown in Fig. (2-1b).

This geometry has a potential solution allowing an infinite summation of Legendre functions, but the approximation is made that the only term used is that allowed in the conical solution namely $n = 1/2$. This is equivalent to assuming that the equipotential chosen can be defined by $\theta = \theta_o$ at all points except those near the apex. The potential is then given by

$$\phi = \left[\frac{V_o a_1^{1/2}}{a_1^{1/2} - a_o^{1/2}}\right]\left[1 - \frac{r^{1/2}}{a_1^{1/2}} P_{1/2}(\cos\theta)\right] \tag{2-8}$$

The corresponding electric field intensity is

$$\mathcal{E} = \frac{V_o}{a_1^{1/2} - a_o^{1/2}}\left[\frac{0.5}{r^{1/2}} P_{1/2}(\cos\theta)\hat{a}_r - \frac{\sin\theta}{r^{1/2}} \frac{(P_{1/2}(\cos\theta))}{(\cos\theta)} \hat{a}_\theta\right] \tag{2-9}$$

Hence, the electric field intensity at the tip of the modified conical surface is

$$\mathcal{E}(a_o, o) = \frac{0.5\, V_o}{a_o^{1/2} a_1^{1/2} - a_o} \tag{2-10}$$

The next question which arises concerns the relationship between the radius of curvature, p, of the equipotential ($r^{1/2} P_{1/2} \cos\theta = a_o^{1/2}$) and the radial distance a_o. In spherical coordinates the curvature of a surface is given by

$$K = \frac{1 + \frac{2}{r^2}\left(\frac{dr}{d\theta}\right)^2 - \frac{1}{r}\left(\frac{d^2r}{d\theta^2}\right)}{r\left[\frac{1}{r^2}\left(\frac{dr}{d\theta}\right)^2 + 1\right]^{3/2}} \tag{2-11}$$

The radius of curvature at a point is defined as the reciprocal of the curvature at that point. Evaluating the necessary derivatives on the equipotential surface the radius of curvature at the tip of the modified conical surface is

$$p(a_o, o) = 4a_o \qquad (2\text{-}12)$$

Using Eqns. (2-10) and (2-12) the electric field intensity can be obtained as a function of the radius of curvature at the tip of the modified conical surface

$$\mathcal{E}(p_o, o) = \frac{0.5\ V_o}{\left(\frac{p_o}{4}\right)^{1/2} a_1^{1/2} - \frac{p_o}{4}} \qquad (2\text{-}13)$$

The electric field intensity is plotted for various values of applied voltage at an assumed interelectrode spacing of 0.25 cm in Fig. (2-2).

2.3 Field Evaporation Theory

A sufficiently strong electric field applied to a metallic surface in such a direction as to make the metal positive produces an emission of positive ions. The potential energy of an atom or ion near a metal surface can be approximated by a single curve.(28) If at a given distance from the surface the potential energy can be assumed to be single valued, then energy changes only occur normal to the surface and thermally activated processes can be explained by a one-dimensional energy barrier. Obviously such a model is valid only at distances which are large compared to the dimensions of the surface structure.

The potential energy of an atom as a function of distance x from a surface is shown in Fig. (2-3a). At small distances this curve is dominated by the Pauli exclusion principle and at large distances Van der Waal attractive forces determine the potential. The minimum in the potential energy curve corresponds to the sublimation energy Λ of the atom. The

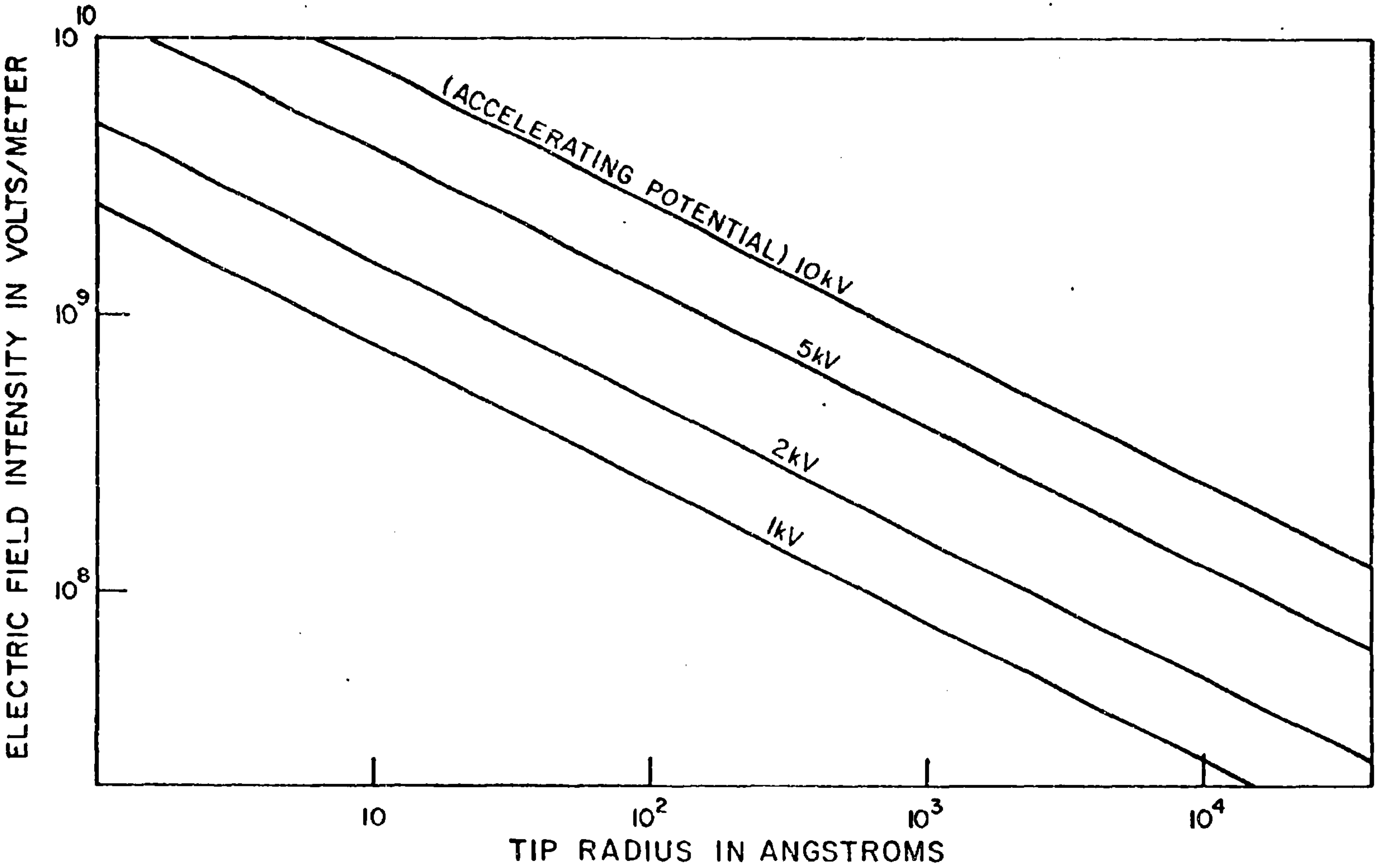

FIG. 2-2 ELECTRIC FIELD INTENSITY AS A FUNCTION OF RADIUS WITH ACCELERATING POTENTIAL AS A PARAMETER

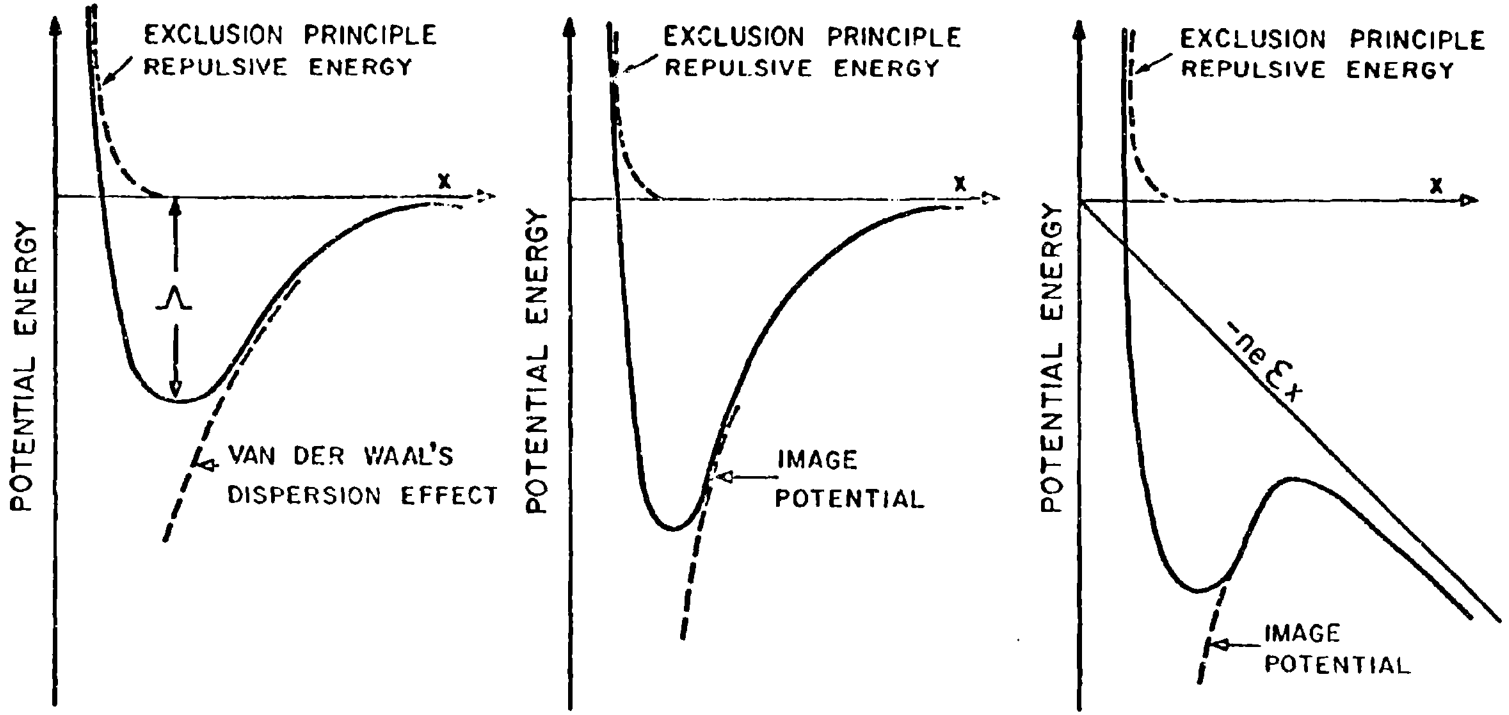

(a) ATOMIC POTENTIAL

(b) IONIC POTENTIAL

(c) IONIC POTENTIAL WITH ELECTRIC FIELD

FIG. 2-3 ATOMIC AND IONIC POTENTIAL ENERGY AS A FUNCTION OF DISTANCE FROM A METALLIC SURFACE corresponding curve for an ion is shown in Fig. (2-3b). The energy needed to ionize an atom in the gas phase is $\sum I_n$ where n is the number of elemental charges of the ion and I_n is the nth ionization potential of the atom. If the electrons produced by the ionization are returned to the metal surface, an energy $n\phi_o$ is recovered. The quantity ϕ_o is the absolute work function of the metal which is the energy difference between an electron at infinity and an electron at the top of the Fermi surface of the metal. The zero level for the potential energy of an ion must therefore be at a distance $\sum I_n - n\phi_o$ above the zero level for the corresponding atom. The potential energy curve for the ion is determined by two effects. Again at small distances the Pauli exclusion principle dominates, but at large distances the ion is attracted by its negative image in the metal (Schottky image potential) and a minimum in the potential curve is produced.

The application of an electric field to the specimen alters the potential energy curve of the ion. The potential energy at any point, x, is reduced by $n\mathcal{E}ex$ where $\mathcal{E}$ is the applied field and e is the charge of an electron. The effect of the electric field is to produce the maximum in the ion potential energy curve shown in Fig. (2-3c). At a distance x from the metal, the ion experiences a Schottky image force

$$F = \frac{-e^2}{4\pi e_o (2x)^2} \qquad (2\text{-}14)$$

where e_o is the capacitivity of free space.

By including the effect of the applied field and assuming that the ion is sufficiently far from the metal to ignore the repulsion potential, the potential energy of the ion is given by

$$U_I(x) = \frac{-e^2}{16\pi e_o x} - ne\mathcal{E}x \qquad (2\text{-}15)$$

The maximum of this potential energy curve can be found by differentiating Eqn. (2-15) with respect to x. The position of the maximum is found to occur at

$$x_{max} = \left[\frac{ne}{16\pi\epsilon_o\mathcal{E}}\right]^{1/2} \qquad (2\text{-}16)$$

and the energy at this maximum is

$$U_I(x_{max}) = \left[\frac{n^3e^3\mathcal{E}}{4\pi\epsilon_o}\right]^{1/2} \qquad (2\text{-}17)$$

which is the image or Schottky hump and is independent of x as long as the repulsion potential can be ignored.

If the ionic potential curve is superimposed on the atomic potential curve several possibilities exist.(29) First, if the ionization potential is sufficiently low, the atom may be adsorbed at the surface as an ion. The ionic potential curve lies below the atomic potential curve, and field evaporation takes place over the image potential hump described by Eqn. (2-17) and shown in Fig. (2-4a). Second, if the ionization potential is higher the atom is adsorbed as a neutral and is ionized when the ionic and atomic curves intersect. If this intersection is to the left of the image hump as shown in Fig. (2-4b), the image potential theory is valid and for either of the above two cases the activation energy for field evaporation Q is given by(20)

$$Q = Q_o - \left[\frac{n^3e^3\mathcal{E}}{4\pi\epsilon_o}\right]^{1/2} \qquad (2\text{-}18)$$

where $Q_o = \Lambda + \sum I_n - n\phi_o$

Third, at still higher ionization potentials the atomic and ionic curves may intersect to the right of the image-potential hump, as shown in Fig. (2-4c), and the image-potential theory is no longer valid. In

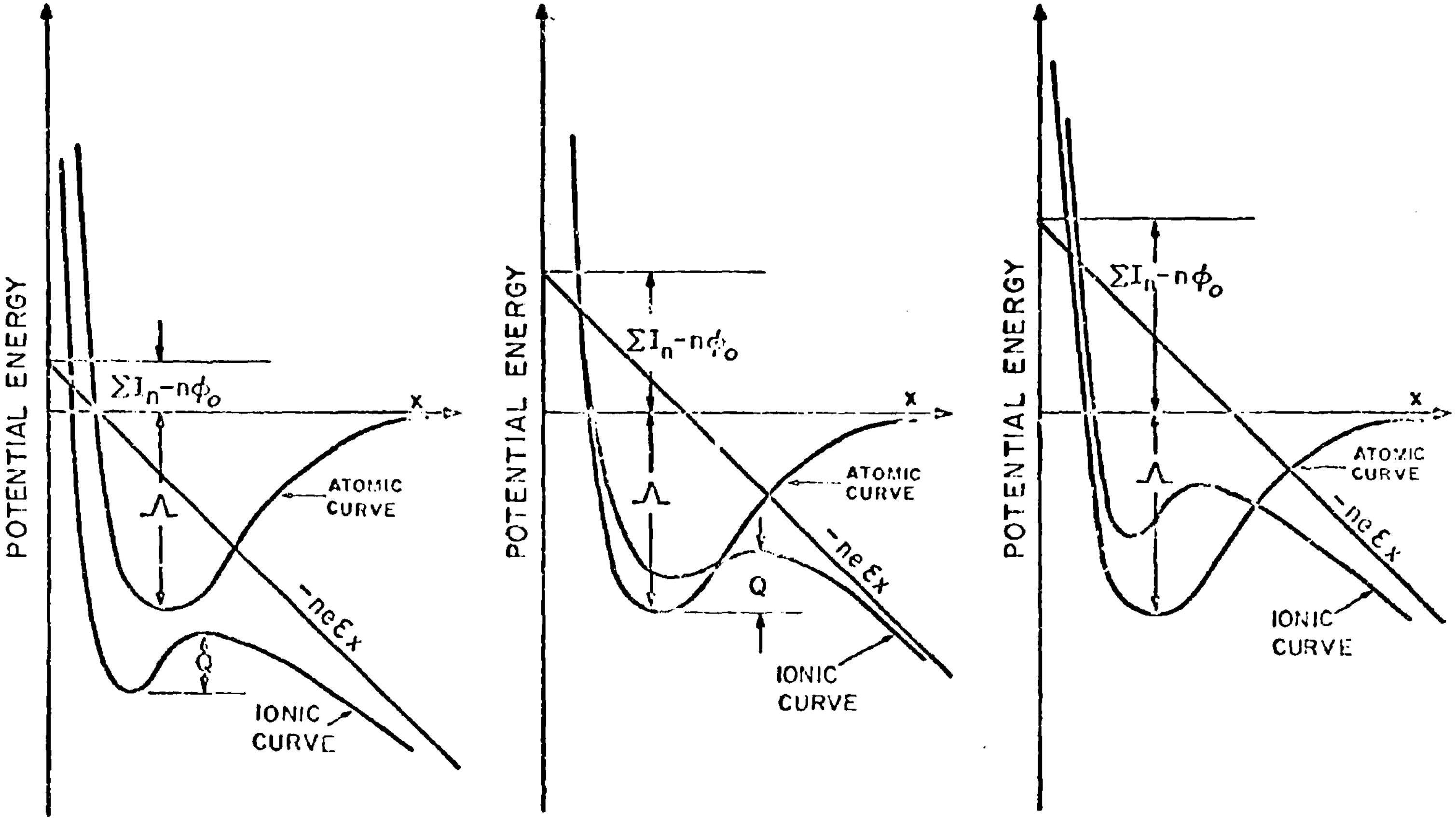

(a) SURFACE IONIZATION (b) IMAGE POTENTIAL (c) INTERSECTION

FIG. 2-4 SUPERIMPOSED ATOMIC AND IONIC POTENTIAL ENERGY CURVES this case the energy maximum does not correspond to the image hump but is approximately given by$^{(29)}$

$$Q = Q_o - ne\mathcal{E}x_c \qquad (2\text{-}19)$$

where x_c is the distance at which the intersection occurs.

The two models for the field evaporation process given by Eqns. (2-18) and (2-19) are referred to as the image-potential and intersection models respectively. One predicts a square root dependence of the activation energy on the applied electric field and the other a linear dependence.

The choice of models depends on the location of the intersection of the ionic and atomic potential curves. The position of the intersection can be approximated by considering the following energy ratio$^{(30)}$

$$X = (\sum I_n - n\phi_o)/\Lambda \qquad (2\text{-}20)$$

For $X<1$ the atoms will probably be adsorbed as ions, for $1<X<3$ the atomic and ionic potential curves will intersect to the left of the Schottky hump; and for $X<3$ the intersection is to the right of the hump.

The energy ratios for gallium and indium are 0.64 and 0.68 respectively for $n = 1$.$^{(30)}$ Consequently, the atoms are either adsorbed as ions or are ionized very near the surface. In either case field evaporation occurs over the image potential hump and Eqn. (2-18) is valid.

Atoms will evaporate from a metal surface because of thermal vibrations with a time constant.

$$\tau = \tau_o \, \mathrm{EXP}(Q/kT) \qquad (2\text{-}21)$$

where τ_o is the reciprocal of the Einstein frequency of the bound particles, Q is the energy hump that has to be overcome by the vibrational excitations, k is Boltzmann's constant, and T is the temperature. Substituting Eqn. (2-18) into the above, the time constant for evaporation under the influence of an electric field is then given by

$$\tau = \tau_o \, \mathrm{EXP}\left(\frac{Q_o - \left(\frac{e^3\mathcal{E}}{4\pi e_o}\right)^{1/2}}{kT}\right) \qquad (2\text{-}22)$$

The total current emitted by field evaporation is equal to the current per source multiplied by the number N of lattice sites undergoing evaporation.

$$I = \frac{Ne}{\tau} \qquad (2\text{-}23)$$

From Eqns. (2-22) and (2-23) the emitted current can be found as a function of the applied electric field.

$$I = \frac{Ne}{\tau_o} \, \mathrm{EXP}\left(\frac{\left(\frac{e^3\mathcal{E}}{4\pi e_o}\right)^{1/2} - Q_o}{kT}\right) \qquad (2\text{-}24)$$

As the electric field intensity is increased, the current increases due to two simultaneous effects. First, the time constant for evaporation decreases; and second, the number of sites contributing to the total current output increases.

2.4 Energy Loss in Ion Beam Formation

Many possible loss mechanisms exist in the production of charged particle beams by field evaporation. Three sources of loss will be examined: (1) The binding energy of the evaporated atoms; (2) Ohmic losses in the liquid meniscus; and (3) Space charge effects.

A. Binding Energy

The energy necessary to field evaporate an atom as given by Eqn. (2-18) is composed of three terms. The height of this energy hump is equal to the sublimation energy of the atom, plus its ionization energy, minus the electron activation energy. Therefore, the ions are not accelerated through the entire potential applied to the surface. A fraction of this energy is required to produce the particles. The potential that is needed to produce an ion is given by

$$V_f = eQ_o \tag{2-25}$$

where Q_o is the energy required to create an ion. For both Gallium and Indium Q_o is less than 5 ev; hence, the potential drop V_f is insignificant compared to the kinetic energy that the ions acquire.

B. Ohmic Losses

The finite conductivity of the working fluid produces a non-zero value of resistance in the spraying meniscus. The physical conical meniscus has a finite radius apex.

This geometry can be approximated by a truncated cone. The resistance of such a conical volume is given by

$$R = \rho \int_{r_1/\tan\alpha}^{r_2/\tan\alpha} \frac{dz}{\pi z^2 (\tan\alpha)^2} \qquad (2\text{-}26)$$

where ρ is the resistivity of the working fluid, α is the semivertical angle of the conical surface, z is a "dummy" variable of integration, and r_1 and r_2 are the minimum and maximum radii of the conical surface respectively.

Equation (2-26) is easily integrated and assuming $r_1 << r_2$, the following expression is obtained for the resistance of the truncated cone.

$$R = \frac{\rho}{r_1 \pi (\tan\alpha)} \qquad (2\text{-}27)$$

For the Gallium-Indium eutectic working fluid and a semivertical angle of 49.3°, Eqn. (2-27) becomes

$$R = \frac{8.1\text{x}10^{-6}}{r_1} \qquad (2\text{-}28)$$

The potential drop in the liquid is then given as the product of the emitted current and the resistance of the meniscus

$$V_z = IR \qquad (2\text{-}29)$$

For a current of 500 μA and minimum radius of 10^{-8} meter, the resulting potential drop is less than one volt. Consequently, for the Gallium-Indium working fluid ohmic losses are negligible.

C. Space Charge Effects

The presence of positive charges in the vicinity of the field evaporating surface alters the potential distribution of the applied field. Since a charge placed in a volume already containing a net charge density possesses a well defined potential energy, it is necessary for the emitted particles to convert some of their available kinetic energy into potential energy in order to be placed into the beam. To find the magnitude of this potential barrier, it is assumed that the emitted positive particles form a cylindrical beam with a constant current density J over its cross-sectional area.

The current density J, volume charge density ρ, and particle velocity v are related by

$$J = \rho v \tag{2-30}$$

The particle velocity in turn is related to the accelerating potential by Eqn. (1-2). Poisson's equation in cylindrical coordinates can be written in the form

$$\frac{d^2V}{dr^2} + \frac{1}{r}\frac{dV}{dr} = -\frac{J}{e_o}(2q_sV)^{-1/2} \tag{2-31}$$

This equation can be solved more easily by normalizing the variables V and r.(33) Let the potential at the center of the beam be V_c, and the potential at any other radius be $V_c + V(r)$. The potential may be written in a dimensionless form

$$\frac{V}{V_c} = 1 + W \tag{2-32}$$

where $W = v(r)/v_c$.

Using the normalized potential, Poisson's equation becomes

$$\frac{d^2W}{dr^2} + \frac{1}{r}\frac{dW}{dr} = - \frac{J(2q_s)^{-1/2}}{\epsilon_o V_c^{3/2}} (1 + W)^{-1/2} \qquad (2\text{-}33)$$

The radial coordinate may also be put in a dimensionless form by making the correspondence $R = r/g$, where g is suitable normalizing radius defined by

$$g^2 = \frac{\epsilon_o V_c^{1/2}(2q_s)^{1/2}}{J} \qquad (2\text{-}34)$$

Hence, the transformed Poisson equation can be written as

$$\frac{d^2W}{dR^2} + \frac{1}{R}\frac{dW}{dR} = - (1 + W)^{-1/2} \qquad (2\text{-}35)$$

Since there is no simple closed form solution to Eqn. (2-35), it is solved most easily by a power series expansion. Noting that W is zero at $R = 0$, and that W is symetric with respect to R, one can assume a solution of the form

$$W = b_2R^2 + b_4R^4 + b_6R^6 + \ldots \qquad (2\text{-}36)$$

Substituting the above expansion into Eqn. (2-35) and expanding the right hand side, the solution obtained is

$$W = - \frac{R^2}{4} (1 + \frac{R^2}{32} + \frac{R^4}{2304} + \ldots \qquad (2\text{-}37)$$

For $R^2 < 0.1$ the first term of this series approximates the true solution to an accuracy of greater than 99%. The increase in potential, due to space charge at the center of the positive ion beam, relative to the perimeter of the beam is given by

$$V_B = \frac{I}{4\epsilon_o(2q_s V_c)^{1/2}} \qquad (2\text{-}38)$$

Hence, to first order, the effect of space charge is independent of the beam radius and directly proportional to the total current. For a current of 500 μA, a voltage of 10 kv, and a specific charge of 5×10^5 coul/Kg, the potential due to the space charge is approximately 150 volts. This value is 1.5% of the total assumed potential of 10 kv.

Therefore, in considering the three loss mechanisms discussed in this section it is obvious that only space charge effects would produce measureable energy losses. The effects of the space charge would be to produce a transverse acceleration of the ions in the beam.

3. EXPERIMENTAL TECHNIQUES

The experimental apparatus and instrumentation will be described and relevant design criteria expounded upon. The discussion will be subdivided into three categories: (1) The vacuum system; (2) The EHD spraying apparatus; and (3) The particle detection instrumentation.

3.1 Vacuum System

All experimentation was performed in an ambient pressure of less than 10^{-6} torr that was maintained by an oil diffusion pump and a mechanical roughing and fore pump.

The vacuum chamber consisted of a custom made six inch industrial glass pipe* tee with an additional four inch port mounted perpendicular to the plane of the tee. The three six inch ports available were used for mounting the spraying apparatus, mounting the detection apparatus, and pumping respectively. The four inch port was utilized for an optical monitoring system. A photograph with an accompanying schematic diagram of the experimental set-up are shown in Fig. (3-1).

3.2 Spraying Apparatus

The beam formation equipment consisted of: (1) A set of electrodes composed of the spraying capillary and accelerating electrode; (2) A positive displacement feed system to control the flow of working fluid through the capillary; and (3) The accelerating voltage supplies. The spraying apparatus is shown in Fig. (3-2).

---

* Pyrex "Double Tuff" Brand, Corning Glass Works, Corning, New York

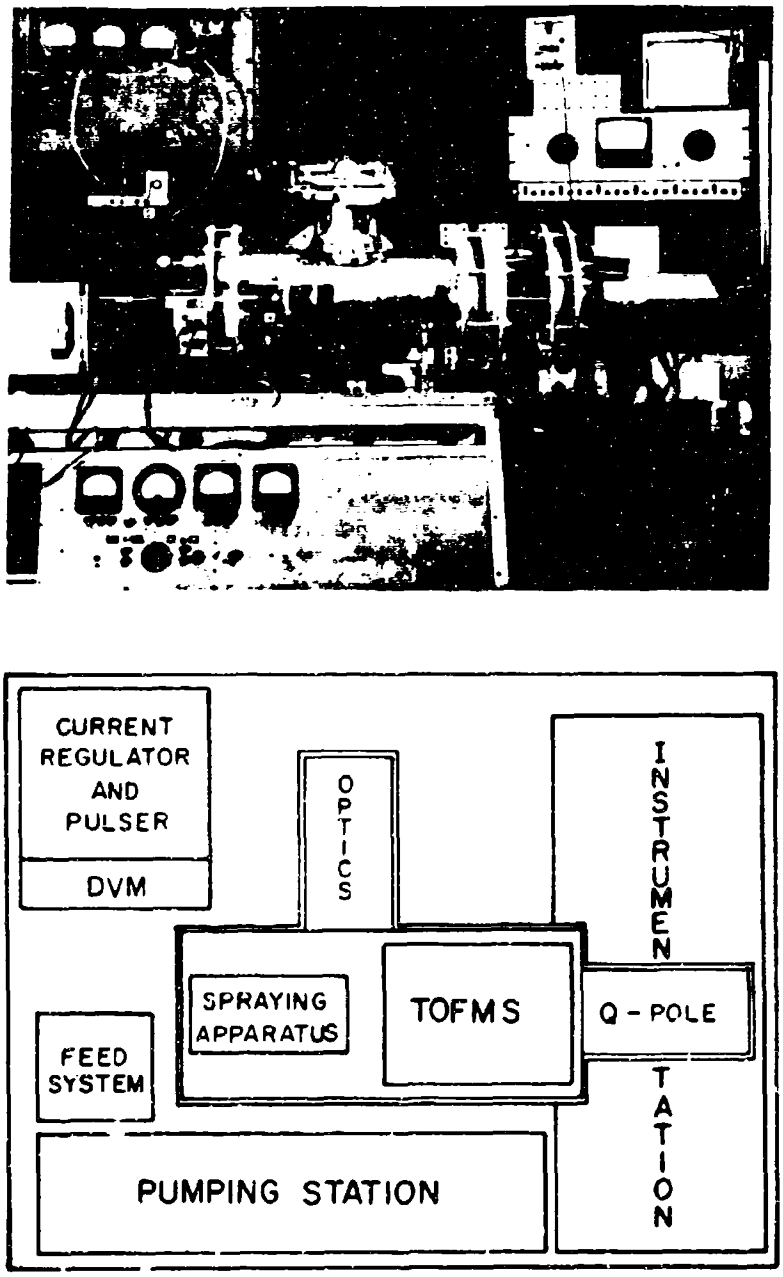

FIG. 3-1 EXPERIMENTAL APPARATUS

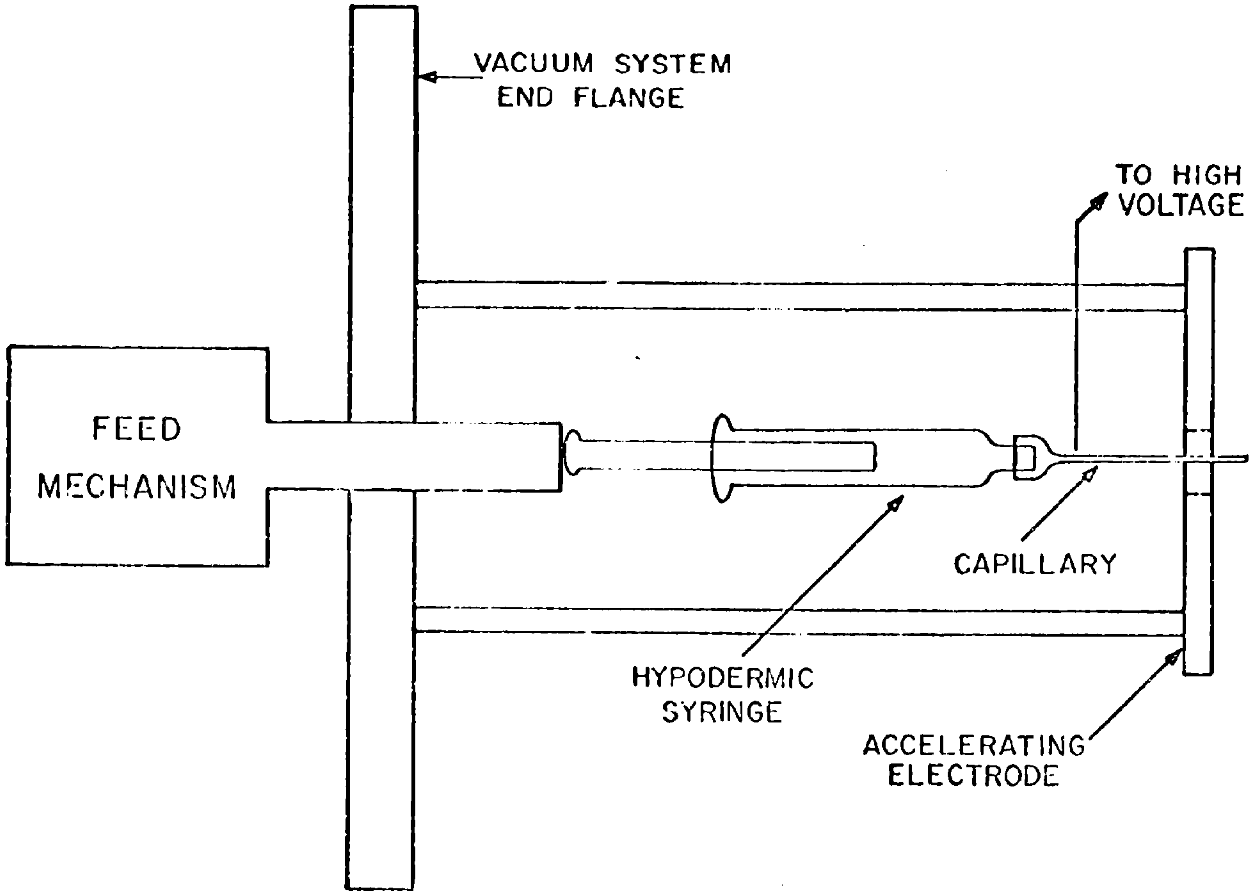

FIG. 3-2 DETAILS OF THE EHD SPRAYING APPARATUS

A. High Voltage Electrodes

The electrode geometry consisted of the capillary (anode) and a concentric, planner accelerating electrode (cathode) through which the capillary protruded. The design of the capillary was paramount to realization of the proper mode of spraying (i.e. field evaporation mode). Relevant design factors included the material, tip finish, and size of the capillary.

The choice of capillary material was based on its susceptibility to wetting by the gallium-indium eutectic. Traditionally, stainless steel capillaries have been employed in most EHD spraying experiments because of their ease of fabrication and accessibility (standard medical type hypodermic needle stock). Unfortunately, the gallium-indium alloy does not properly wet stainless steel. Without sufficient wetting, the predicted conical meniscus is not produced. Instead, as the applied electric field is increased, the entire meniscus is pulled off of the capillary in a large "blob". The desired wetting was achieved by using nickel capillaries(32) that were fabricated from seamless (250 μm OD x 125 μm ID) nickel tubing.*

The tip of the capillary had have a smooth highly polished surface. A small burr on the tip could lead to a locally high electric field and perturb the spray. The raw nickel tubing was cut to approximately the desired length with diagonal cutters. This procedure crimped the ends of the tubing shut. They were then placed in a high speed jewelers lathe. By applying a slight lateral pressure to the rotating tubing, a fatigue crack was produced that eventually ruptured the tubing

---

* Nickel 200 Brand Tubing, Superior Tube Co., Norristown, Pennsylvania

leaving an open end. The spraying tip was then polished with jewelers rouge. A photomicrograph of a finished capillary is shown in Fig. (3-3).

The size of the capillary influenced the stability of the meniscus. As the capillary size was decreased the meniscus became more stable. The lower limit on the capillary size was dictated by the availability of small diameter nickel tubing, the ease of fabrication of the finished capillary, and its resistance to plugging.

B. Feed System

The finished capillaries were cemented into the cannula of a hypodermic needle. This facilitated attachment to a syringe that functioned as a reservoir for the working fluid. The flow of liquid through the capillary was controlled by a positive displacement feed system. The principle components of this system were a guide mechanism and a lead screw that transformed an angular motion into a linear displacement. The lead screw was rotated by a chart recorder drive at speeds as low as 2 revolutions per day. The linear motion produced was transferred to the plunger of the syringe and the resulting mass flow rate could be varied from 10^{-5} to 10^{-11} kg/sec.

C. Supply Voltages

The electric field normal to the conical liquid meniscus must be of sufficient amplitude to support the conical geometry, but not so great that it pulls off the entire meniscus. Because the gallium-indium eutectic is a very good conductor, the meniscus forms the anode of the spraying field geometry, and any motion of the liquid changes the "constant" in the voltage-field relationship. From Eqn. (2-24) it is evident that the spraying current varies greatly with a small change in

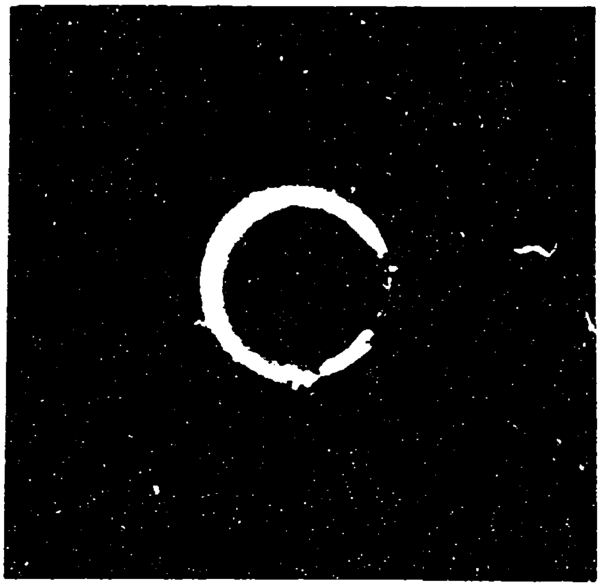

FIG. 3-3 PHOTOMICROGRAPH OF
250 μm O.D. NICKEL CAPILLARY

field strength. Hence, it is necessary to have feedback in the accelerating voltage supply to maintain a constant field (i.e. constant current) independent of changes in the electrode geometry.

The accelerating voltage was obtained from a regulated 30 KVDC supply. The circuit shown in Fig. (3-4) was used to regulate the emission current level by controlling the bias on a series regulator tube. A three digit-digital voltmeter (DVM) was used to monitor the accelerating voltage. The input impedance of the metering circuitry was approximately 1 gigaohm and thus did not effect the current regulation.

The field evaporated ions upon impact with metallic parts in the vacuum system can produce secondary electrons. These secondaries can then be accelerated to the capillary (at a high positive DC potential) and heat it and even melt it shut. By placing the accelerating electrode at a negative bias of 300 volts, any secondaries produced "see" this negative potential instead of the positive capillary potential. (This is because the bias field is fairly uniform and the capillary field decreases rapidly with distance.) Consequently, the secondaries are suppressed, the capillary is not heated, and the measured capillary current is only the ion current.

3.3 Detection Apparatus

The following parameters of the field evaporated particles were to be measured: (1) The beam current as a function of the applied field; (2) The specific charge distribution as a function of the beam current, and (3) The formation energy of the particles as a function of the beam current.

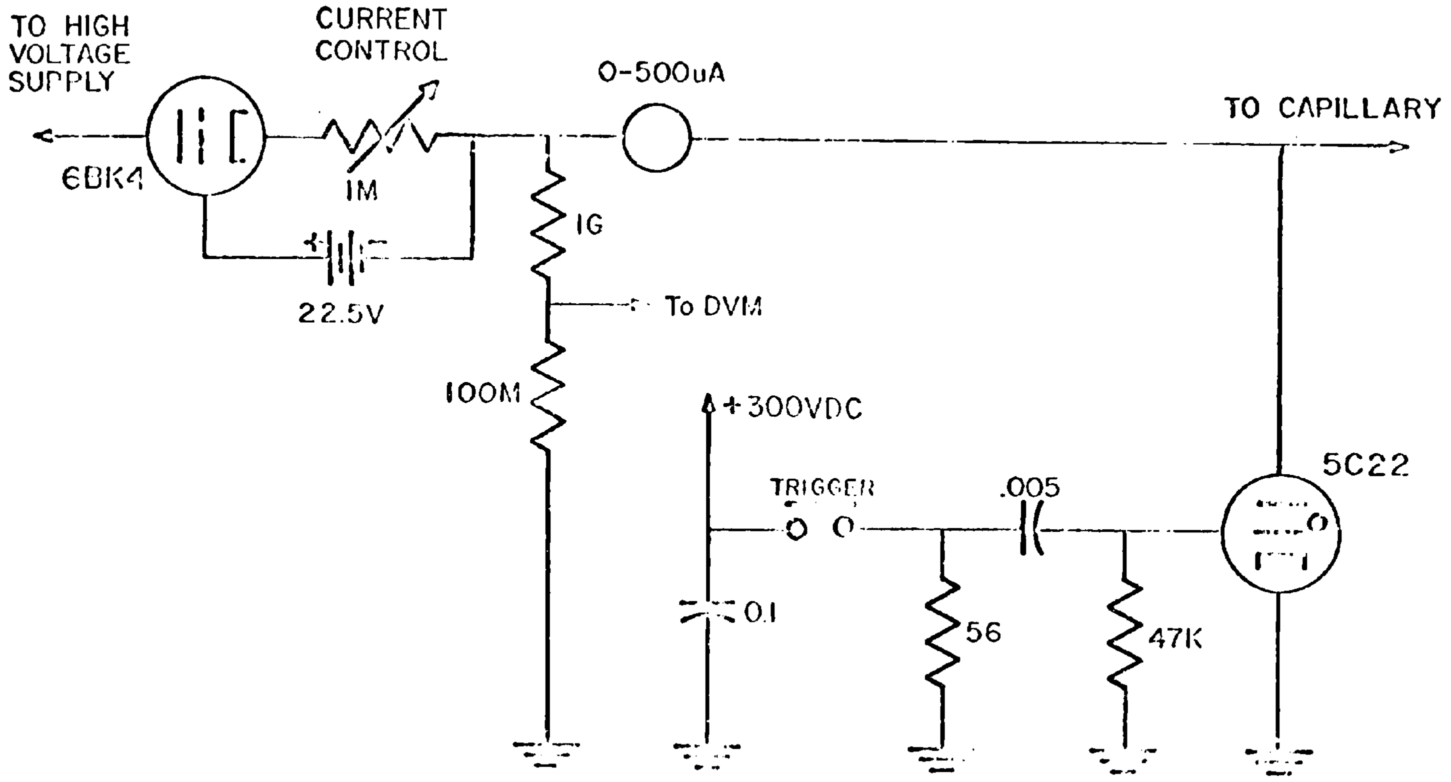

FIG. 3-4 HIGH VOLTAGE CURRENT REGULATOR AND PULSER CIRCUITRY

A. Specific Charge Distribution

The measurement of the specific charge distribution was accomplished by utilizing two specific charge selective instruments. The first, a time-of-flight mass spectrometer (TOFMS) was used because it can detect a large cross-section of the ion beam. Unfortunately, it has low resolution. The second device used was a quadrupole mass filter. It was placed in tandem with the TOFMS and its operation complemented that of the TOF device. The quadrupole detects only those ions very near its axis of symmetry, but it is capable of high resolution. Thus, the simultaneous use of both instruments provided an overall picture of the specific charge distribution. Since both instruments sense the specific charge of the particles and not their mass, the mass spectrum was found by assuming that all particles carried only one elementary charge.

1. Quadrupole Mass Filter

A schematic diagram of the quadrupole mass filter is shown in Fig. (3-5). Physically the device consists of four conducting cylindrical electrodes placed at the corners of a square. This geometry is used to approximate a hyperbolic cross-section that can be easily analyzed. The basic concept of the device is to provide a potential field distribution periodic in time and symmetric with respect to its axis, which will transmit a selected mass group and cause ions of improper mass to be deflected away from the axis. In particular, this mass selection scheme employs a combination of DC potentials plus an RF component such that the transit time of an ion is long compared to the RF period.

The profiles in the xy plane of the idealized hyperbolic electrodes are given by

$$\pm(x^2 - y^2) = r_o^2 \qquad (3\text{-}1)$$

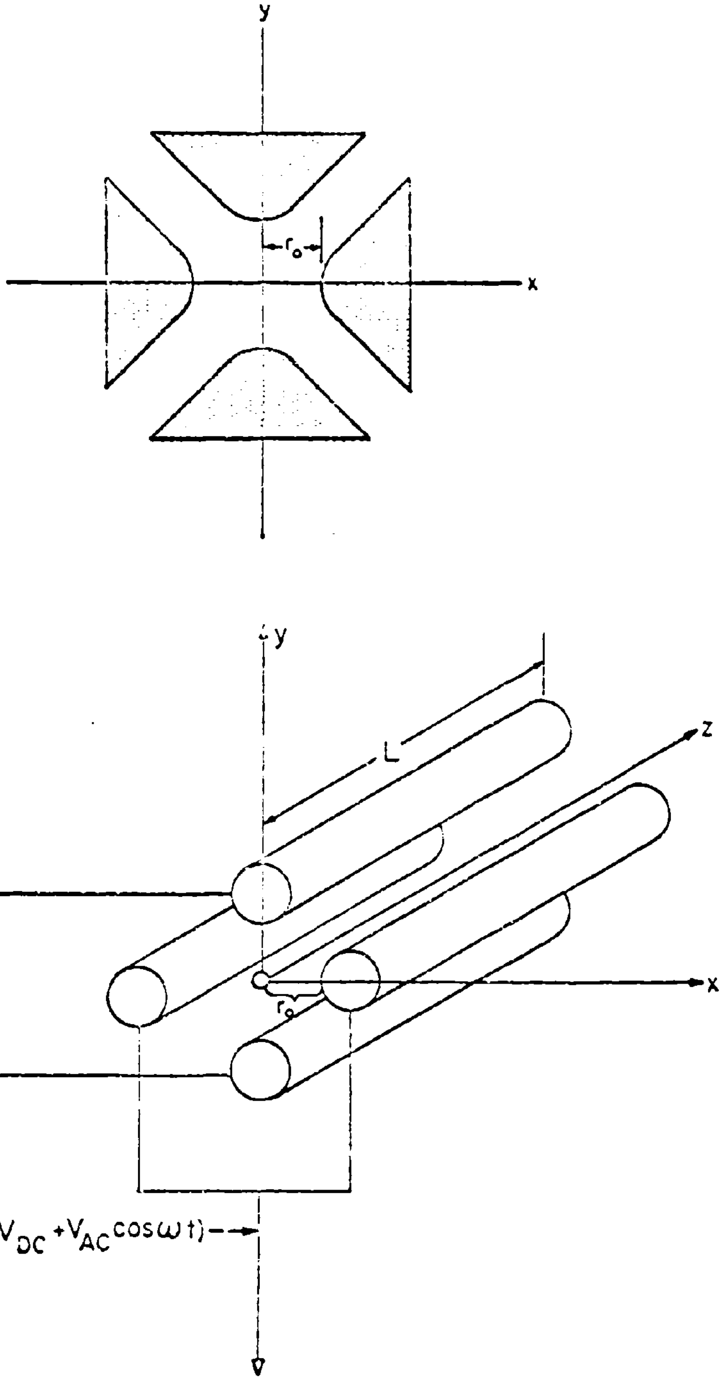

FIG. 3-5 SCHEMATIC DIAGRAM OF QUADRUPOLE MASS FILTER

where r_o is a geometric constant of the device. In general, the voltages applied to the electrodes can be written as

$$V(t) = \pm (V_{dc} + V_{ac}\cos\omega t) \qquad (3\text{-}2)$$

and the corresponding potential distribution in the xy plane is

$$\emptyset(x,y) = (V_{dc} + V_{ac}\cos\omega t)\left[\frac{x^2 - y^2}{r_o^2}\right] \qquad (3\text{-}3)$$

The electric field intensity between the electrodes is then

$$\mathcal{E} = 2(V_{dc} + V_{ac}\cos\omega t)\left[\frac{x\hat{a}_x - y\hat{a}_y}{r_o^2}\right] \qquad (3\text{-}4)$$

The equations of motion of positive ions under the influence of the above electric field are

$$\frac{d^2x}{dt^2} + (V_{dc} + V_{ac}\cos\omega t)\frac{2q_s x}{r_o^2} = 0$$

$$\qquad (3\text{-}5)$$

$$\frac{d^2y}{dt^2} - (V_{dc} + V_{ac}\cos\omega t)\frac{2q_s y}{r_o^2} = 0$$

By making the correspondences

$$\frac{\omega t}{2} = \theta; \qquad \frac{8q_s V_{dc}}{r_o^2 \omega^2} = a; \qquad \frac{4q_s V_{ac}}{r_o^2 \omega^2} = q \qquad (3\text{-}6)$$

the equations of motion are transformed into standard Mathieu's equations

$$\frac{d^2x}{d\theta^2} + (a + 2q\cos 2\theta)\,x = 0$$

$$\qquad (3\text{-}7)$$

$$\frac{d^2y}{d\theta^2} - (a + 2q\cos 2\theta)\,y = 0$$

The general solution of these equations takes an exponential form and there exists finite limits on the ranges of a and q for stable trajectories.

By varying the ratio a/q the resolution of the mass filter is changed. At $a = .236$ and $q = .706$ only one mass number is stable and maximum resolution is obtained.(34) At maximum resolution, the stable mass number A, RF amplitude V_{ac}, and RF frequency ω are related by

$$V_{ac} = 7.21\ f^2(\mathrm{MHz})\ r_o^{\,2}(\mathrm{cm})\ A \tag{3-8}$$

Therefore, by measuring the amplitude of the RF voltage and its frequency at a particular operating point, the stable mass number is determined.

The quadrupole mass filter was fabricated from 0.250 inch diameter centerless ground stainless steel rods 40 cm long. They were end supported by 0.125 inch diameter synthetic sapphire ball bearings. This support system allowed for precise alignment of the rods and provided electrical isolation. The entire assembly was placed in a conducting cylinder to shield the RF voltages.

The power supply for the quadrupole is shown in Fig. (3-6). A basic Ecceles Jordan configuration was used with a tuned circuit plate load to produce a double ended oscillator, operating at approximately 2 MHz. The RF signal obtained was stepped up to 3 KV peak amplitude by an air core inductor. The DC bias for the quadrupole was obtained by rectifying a part of the RF signal and then adding it back to the RF in the output stage.

The stable mass number of the quadrupole can be varied by varying either the RF amplitude or RF frequency. Amplitude sweeping was chosen because of its simplicity. A block diagram of the quadrupole instrumentation is shown in Fig. (3-7). The plate voltage for the quadrupole supply was obtained from a programmable power supply. By applying a ramp input to the supply, the plate voltage could be swept and hence the RF output

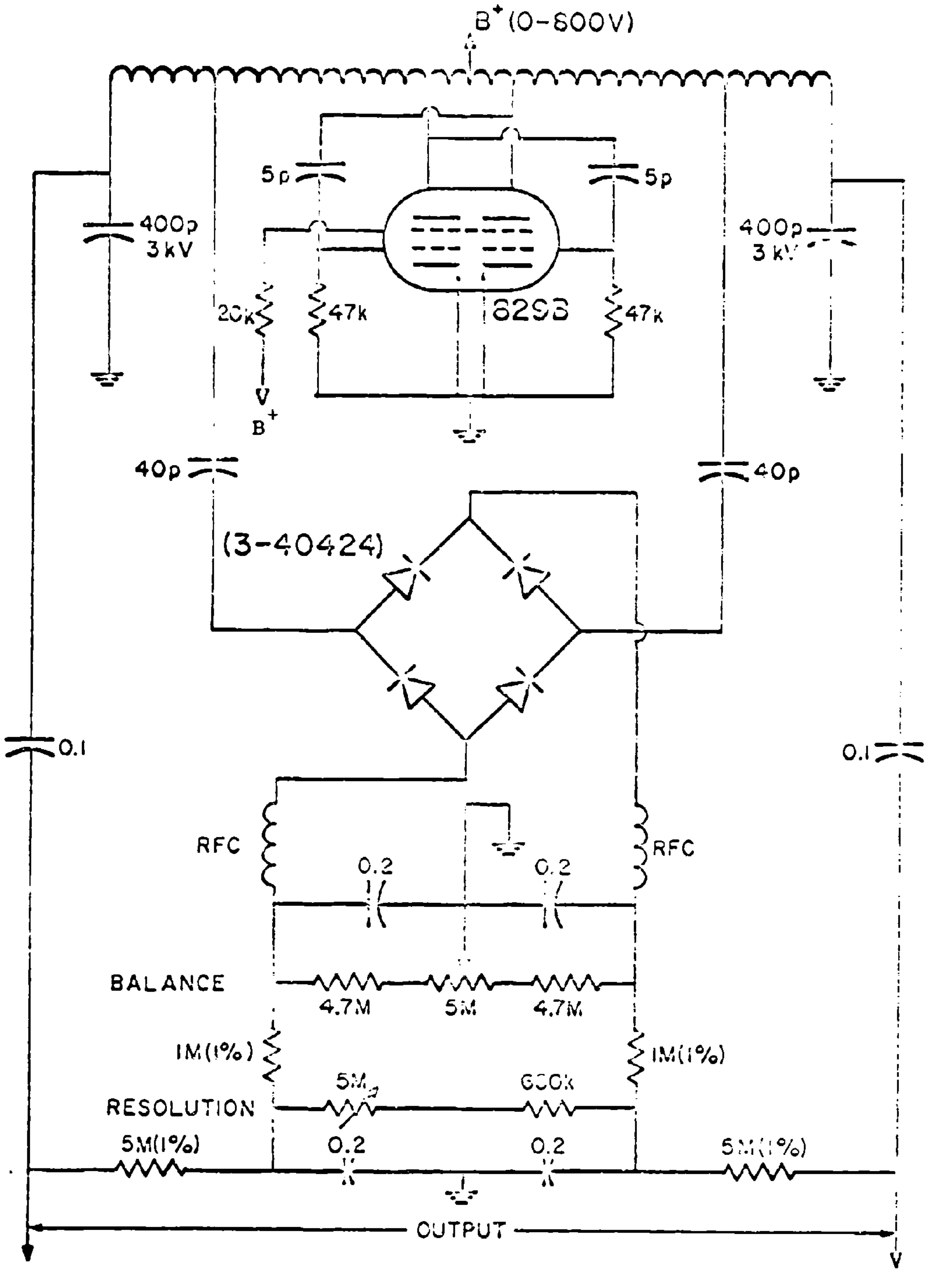

FIG. 3-6 QUADRUPOLE MASS FILTER POWER SUPPLY CIRCUITRY

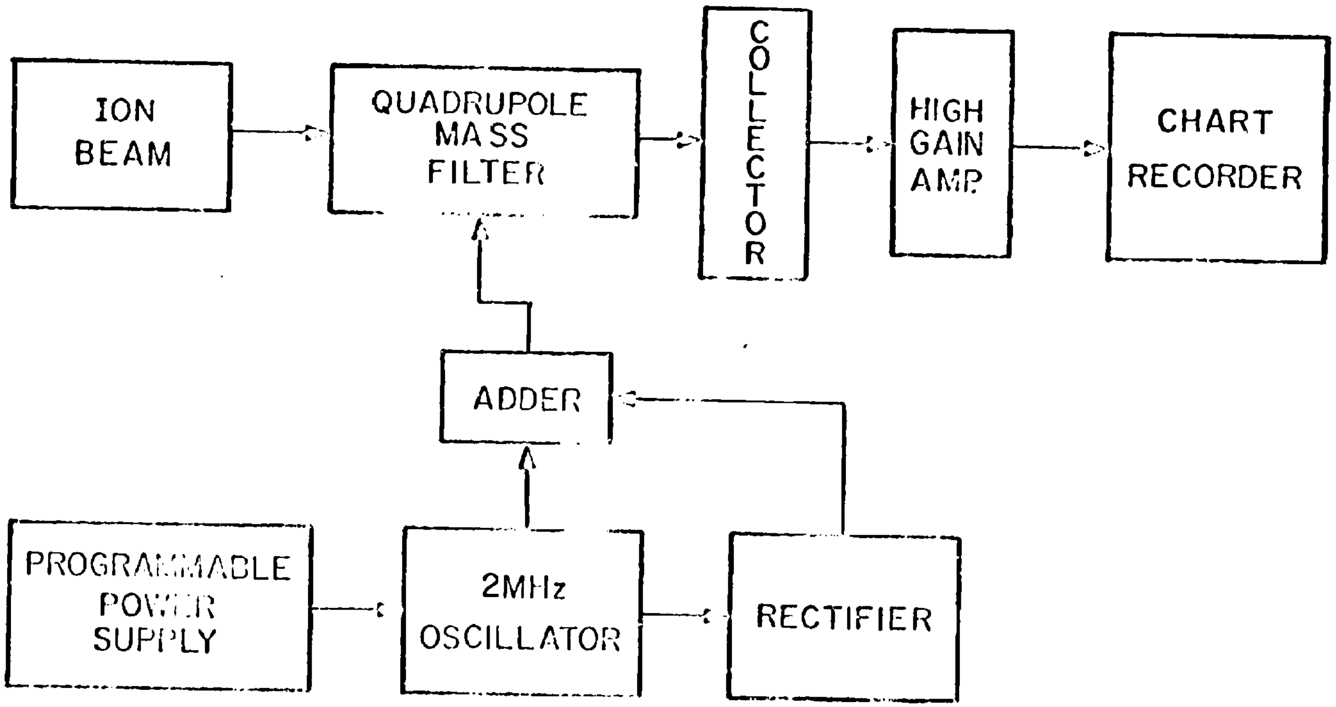

FIG. 3-7 **BLOCK DIAGRAM OF QUADRUPOLE MASS FILTER INSTRUMENTATION**

could be varied to cover a range of stable mass numbers ranging from 1 to 420. The ion current passing through the quadrupole was amplified by a high gain electrometer circuit and the output of the electrometer was used to drive a strip chart recorder.

2. Time of Flight Mass Spectrometer

The TOFMS functions by making possible the determination of the transit time of an ion passing through a field free drift space. Ions transverse the drift space with a velocity related to their specific charge and accelerating potential by Eqn. (1-2).

If the ions are all accelerated through the same potential, and the drift space is of length L, the difference in transit time Δt for two ions of masses m_1 and m_2 is

$$\Delta t = \frac{L(m_1^{1/2} - m_2^{1/2})}{(2eV_a)^{1/2}} \qquad (3\text{-}9)$$

In order to measure the transit times of the individual ion species it is necessary to establish a time base. This is accomplished by pulsing off the ion beam and monitoring the beam current. The total beam current is given by(35)

$$I = \int_0^{\infty} i(t_d)\, dt_d \qquad (3\text{-}10)$$

where $i(t_d)$ is the probability density of the current as a function of drift time.

The current density as a function of drift time is the derivative of the collective current

$$i(t_d) = \left.\frac{dI}{dt}\right|_{t_d} \qquad (3\text{-}11)$$

The current density as a function of the specific charge (specific charge distribution) is related to the current density as a function of drift time by

$$i(q_s) = i(t_d)\left(\frac{dt_d}{dq_s}\right) \qquad (3\text{-}12)$$

Accordingly, the specific charge distribution can be obtained by differentiating the beam current waveform.

A schematic diagram of the TOFMS is shown in Fig. (3-8). The collector was formed with a spherical surface with a radius of 25 cm corresponding to the collector-capillary separation. This arrangement provides analysis of all ions sprayed into a cone of approximately 30° apex angle. Ions sprayed at a greater angle hit the surrounding shield. These ions could suffer elastic collisions with the shield and still hit the collector, or they could produce secondary electrons upon impact. To shield the collector from rebounding ions and/or secondary electrons a shield is placed between the capillary and the collector with an aperature of proper size so that all primary particles outside the cone of detection are blocked from the collector.

The third element of the TOFMS is an electrically floating fine wire grid placed near the collector, that shields it from the capillary. By biasing this grid negative it also functions to suppress secondary electrons produced by ion bombardment of the collector surface.

The ion beam was pulsed off by shunting the accelerating voltage to ground potential with a high voltage thyratron. The pulser network is shown in Fig. (3-4). The fall time of the resulting pulse was typically less than 0.1 microsecond and was much less than the average ion drift time of 2.5 microseconds. The length of the pulse was also important.

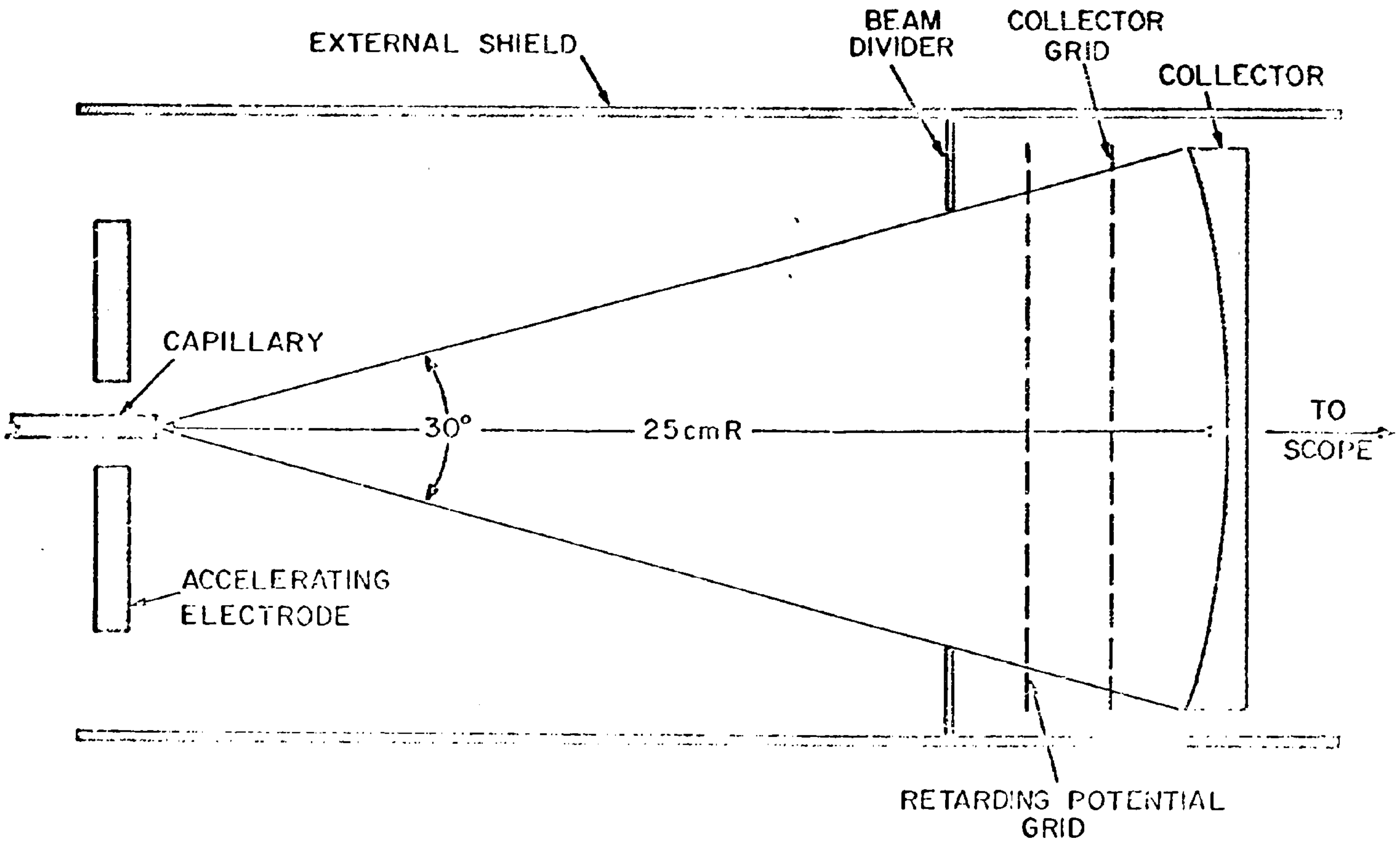

FIG. 3-8 SCHEMATIC DIAGRAM OF TOFMS AND RETARDING POTENTIAL CELL

Since the feed system ran continuously, a long accelerating voltage pulse-off could produce an excess of mass at the capillary and disrupt the spray. This problem was circumvented by making pulses of relatively short duration typically less than 10 ms. This was accomplished by limiting the current through the thyratron to a value less than its holding current. In this mode of operation, the thyratron will remain "on" only as long as its grid is biased positive. Thus by pulsing the grid, the "on" time could be controlled.

The collector current was monitored by a cathode ray oscilloscope with a 33 MHz bandwidth. The capacitance of the collector, cabling, and oscilloscope input was approximately 100 pf. To utilize the fast rise time of the oscilloscope the collector was shunted to ground with a 1000 ohm resistor to keep the time constant of the circuit as low as possible.

Data was taken by pulsing the accelerating voltage and simultaneously triggering the oscilloscope. The decay of the collector current as a function of time was recorded by an oscilloscope camera. The recorded current curve was numerically differentiated to obtain the specific charge distribution.

B. Formation Energy Measurement

The energy distribution of the field evaporated ions was measured with a retarding potential analyzer. The basic principle of the cell is to produce a potential barrier of sufficient height so that ions with energy lower than the barrier are deflected and ions with higher energies pass unaffected.

The physical retarding potential cell utilized the TOFMS drift space.

An additional grid was inserted between the capillary and the collector on to which the retarding potential could be applied, as shown in Fig. (3-8). The retarding potential was supplied by a highly regulated DC supply and measured to an accuracy of 1 volt. The capillary voltage was measured with a digital voltmeter that was calibrated by the retarding potential supply to an accuracy of 10 volts.

If the energy distribution of the field evaporated particles is given by the function F(E), the current to the collector is equal to

$$I = \int_{qV_R}^{\infty} F(E)\, dE \qquad (3\text{-}13)$$

where V_R is the retarding potential.

Therefore, the energy distribution is given by the derivative of the collector current.

$$F(E) = -\frac{dI}{d(qV_R)} \qquad (3\text{-}14)$$

Retarding potential data was obtained by monitoring the collector current with a high resolution, electronic microammeter. Current readings were taken at 10 volt increments in the retarding potential. The resulting current-voltage characteristics were then numerically differentiated to obtain the energy distribution function.

4. EXPERIMENTAL RESULTS

Various measurements were made of the parameters of the field evaporation mode of EHD spraying. These data were taken for two purposes: (1) to corroborate the theory explaining this physical phenomenon proposed in Chapter 2; and (2) to determine the overall efficiency and usefulness of this technique as a source of charged particles for microthruster utilization.

Photomicrographs of the capillary and liquid meniscus were made under all operating conditions to aid in analyzing the operation of the ion source, and to determine the stability of the Taylor cone. The current-voltage characteristic of the emitted ions was determined and used to support the field evaporation theory set forth. The formation energy of the particles was measured at various current levels in order to determine the loss mechanisms in the particle production.

The usefulness of the field evaporation source as a microthruster was determined by analyzing the specific charge distribution of the emitted particles as a function of the capillary current. Using this data and the current-voltage characteristic, the thrust and beam conversion efficienc[illegible] the source could be determined. Likewise, the formation efficiency could be deduced from the retarding potential data.

4.1 Stabilization of the Taylor Cone

The field evaporation mode of EHD spraying was experimentally observed to occur whenever the Taylor cone was produced. The formation of the cone was always accompanied by an emission of ions from its apex. Unstable operating points resulting in oscillations of the conical meniscus produced large lowly charged particles. The cone could be easily reproduced and was indefinitely stable as long as the design criteria outlined in Chapter 3 were maintained. The two most important parameters affecting the formation of the cone were the wetting of the capillary and the feedback control (current regulation) of the accelerating voltage.

The nickel capillaries promoted wetting by the gallium-indium alloy and were pre-wet with the alloy prior to insertion in the vacuum system. Once proper wetting was achieved the capillary remained wetted unless the field was allowed to evaporate off all of the working fluid.

The effect of wetting can be seen in the sequence of photomicrographs shown in Fig. (4-1). A 250 μm O.D. nickel capillary is shown in Fig. (4-1a). In Fig. (4-1b) a sphere of working fluid has been created at the tip of the capillary by the feed system. It does not wet the capillary and thus does not flow back around it. The applied electric field distorts the sphere and tries to pinch it off. This pinching effect reduces the minimum circumference of the liquid meniscus and hence reduces the surface tension forces at that point allowing for further pinching and the eventual breakoff of a large lowly charged droplet.

Microphotographs of the same capillary after induced wetting are shown in Fig. (4-1c). In this case the surface tension forces stabilizing the meniscus act between the capillary and the working fluid. As the field distorts the meniscus the surface tension forces remain constant and support the field. Further increases in the field strength can then produce the Taylor cone.

The regulation of the accelerating voltage had a pronounced effect on the stability of the meniscus. The system was started up by operating

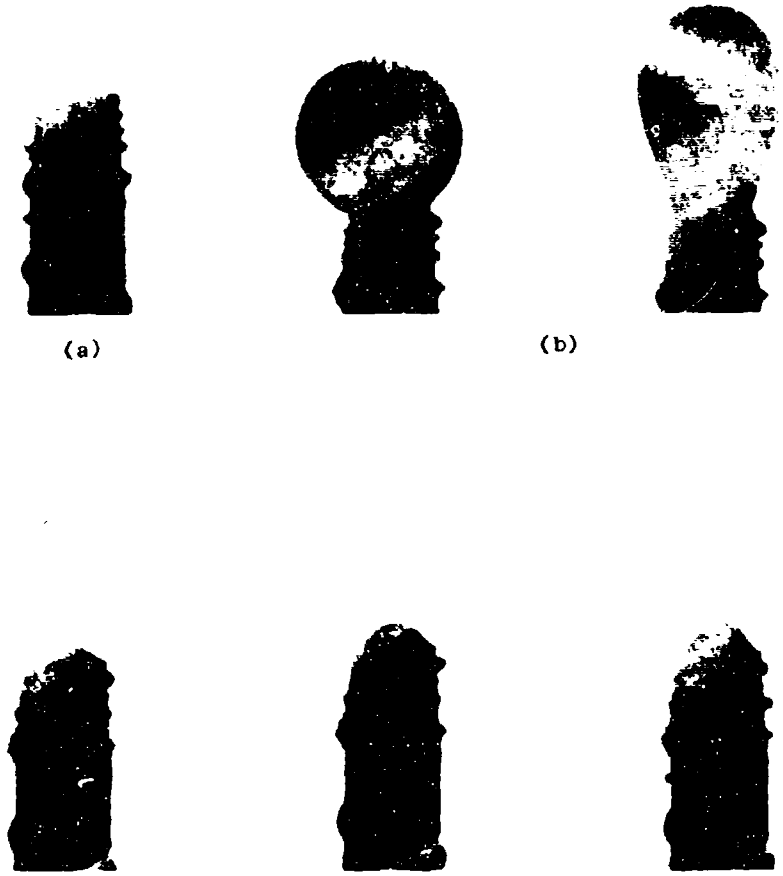

(a) (b)

(c)

FIG. 4-1 EFFECT OF CAPILLARY WETTING. (a) BARE 250 μm O.D. NICKEL CAPILLARY. (b) SHAPE OF MENISCUS WITHOUT WETTING. (c) SHAPE OF MENISCUS WITH WETTING.

the feed system until a hemispherical meniscus appeared at the capillary tip. This meniscus usually had a larger volume than that needed for the stable conical geometry and, therefore, the meniscus would become unstable and large particles with low specific charge would be ejected until the proper volume of working fluid remained. In this mode of operation, the application of an unregulated accelerating voltage would result in the disruption of the entire meniscus. By use of current regulation the instability could be controlled until a stable emission was obtained. In this mode of operation, the accelerating voltage was continuously varying over a dynamic range of approximately 2 KV.

By changing the feedback resistance in the current regulator circuit the capillary current could be continuously varied from 20 to 500 microamps. Once the conical meniscus was stabilized, the applied voltage would remain constant to within 100 volts at a constant current level. Without the regulation it was necessary to compensate manually for the slightest movement in the meniscus in order to keep a steady current level. Thus, the current regulation was found to aid in stabilizing the meniscus and to increase the dynamically stable range of emitted currents.

In Fig. (4-2a) the emitted current from a stable meniscus is shown. The current waveform was obtained by monitoring the particles impinging on the TOF collector by means of an oscilloscope. Photomicrographs of the capillary and stable meniscus are shown in Fig. (4-2b). Apex angles ranging from 60 to 110 degrees were detected. At low current levels (approximately 50 microamps) conical meniscuses with apex angles very near to Taylor's predicted value of 98.6° were observed. At higher current levels the meniscus usually had a smaller apex angle.

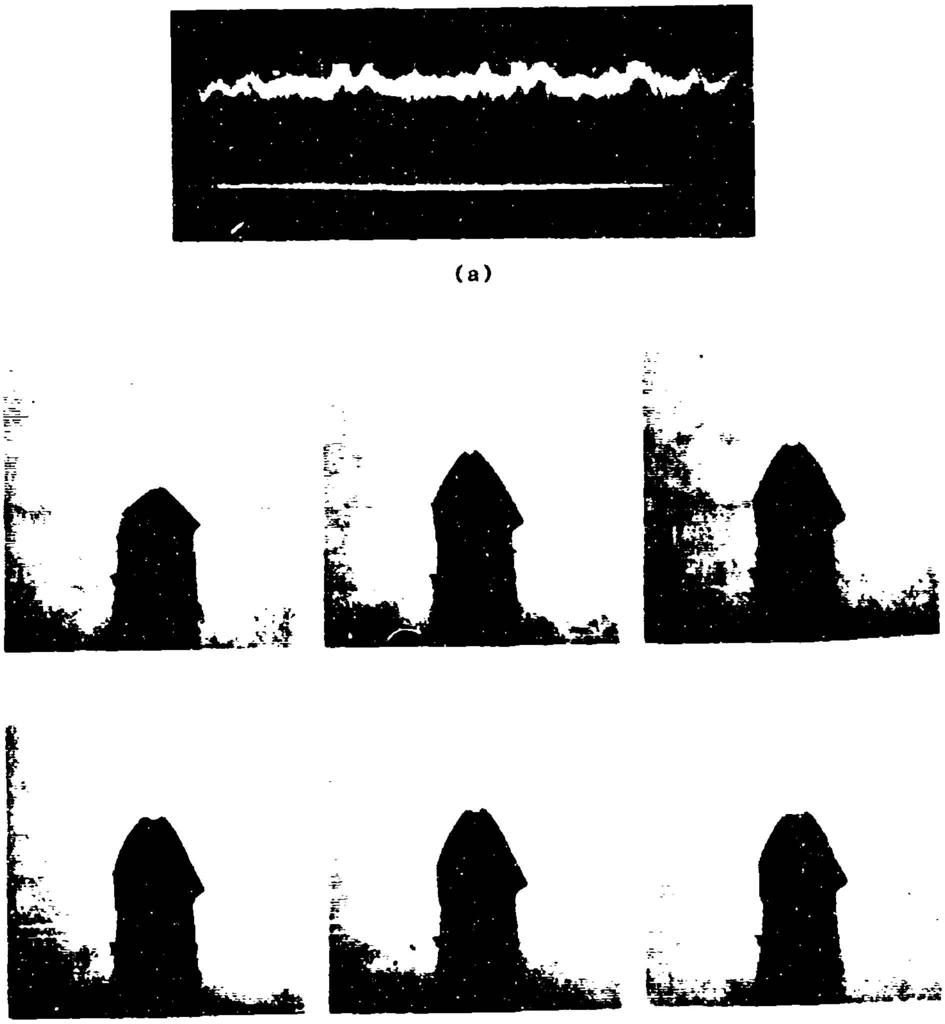

(a)

(b)

FIG. 4-2 STABLE ION EMISSION. (a) EMITTED CURRENT WAVEFORM AT 5 μs/cm SWEEP SPEED. (b) PHOTOMICROGRAPHS OF MENISCUS AT 50, 100, 200, 300, 400, and 500 μA EMITTED CURRENT.

4.2 Capillary Current Measurement

The capillary current was measured with a 0-500 microamp meter placed near the capillary to reduce the possibility of leakage currents. The field evaporation theory developed in Chapter 2 predicts that the logarithm of the emitted current varies as the square root of the applied field. To verify this relationship it was necessary to obtain the functional dependence of the emitted current on the applied voltage. The current-voltage (I-V) characteristic was experimentally determined by measuring the current and voltage at 10 microamp intervals and is plotted in Fig. (4-3) for currents ranging from 20 to 500 microamps. By plotting the logarithm of the current as a function of the square root of the voltage the predicted theoretical relationship is a straight line.

The experimental I-V relationship is divided into three regions: (1) Space charge limited; (2) Emission Limited; and (3) Saturation limited. At low currents and low accelerating voltages the ion emission is space charge limited and the I-V characteristic approximately follows the three-halves power law. At 100 microamps, the capillary current enters an emission limited region. In this mode of operation the I-V characteristic given by a least-squares-error fit to the data points is

$$I = 0.99 \times 10^{-30} \, \mathrm{EXP}(0.75 \, V^{1/2}) \qquad (4\text{-}1)$$

In the range of 100 to 300 microamps the number of lattice sites undergoing evaporation remains essentially constant and the increase in ion current is produced by decreasing the time constant for evaporation at those sites. Hence, the nearly exponential I-V relationship results.

Above 300 microamps the source begins to saturate. Additional

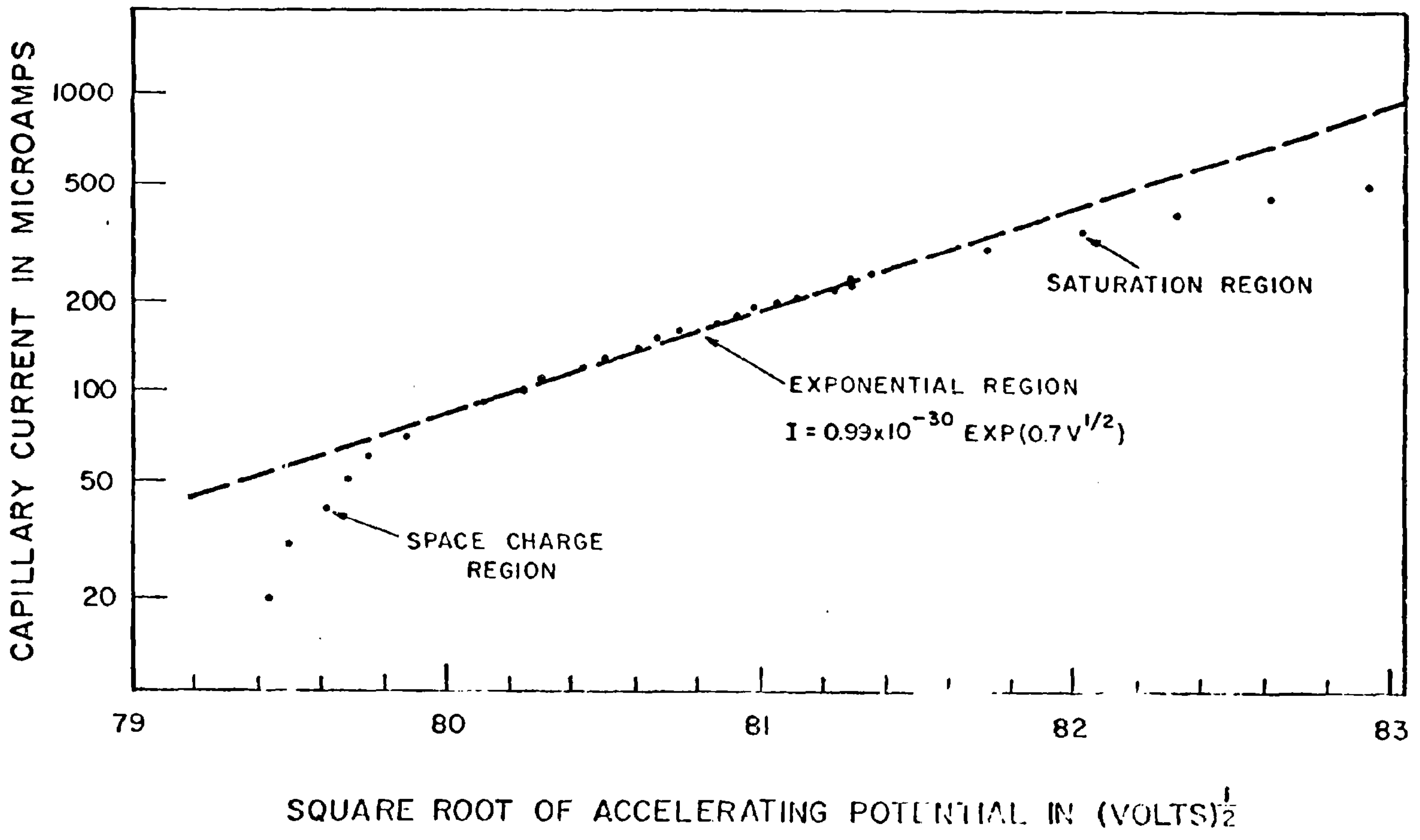

FIG. 4-3 EXPERIMENTAL CURRENT-VOLTAGE CHARACTERISTIC

increases in beam current require additional sites to undergo evaporation. As the number of evaporating sites increases the radius of curvature at the new sites increases; and hence, the voltage necessary to produce the required evaporating field strength increases. This results in a deviation in the I-V curve from the exponential at high current levels.

By considering the exponential region of the I-V curve, the radius and binding energy of the emitting surface can be obtained. After inserting the numerical values for the physical constants at 300° K, the theoretical I-V dependence given by Eqn. (2-24) is

$$I = 1.6 \times 10^{-6} N \, EXP(-40Q_o) \, EXP(1.5 \times 10^{-3} \mathcal{E}^{1/2}) \qquad (4\text{-}2)$$

By equating the coefficients of the exponentials of Eqns. (4-1) and (4-2), the binding energy at the liquid surface can be obtained.

$$0.99 \times 10^{-30} = (1.6 \times 10^{-6}) \, N \, EXP(-40Q_o) \qquad (4\text{-}3)$$

In order to solve for the binding energy, Q_o, the number of lattice sites undergoing evaporation, N, must be determined. For an exponential I-V characteristic, N must be constant throughout the range of operation. The maximum current that can be emitted from a single lattice site is given by Eqn. (2-23) assuming $\tau_o = 10^{-13}$ seconds.

$$I = \frac{e}{\tau_o} = 1.6 \times 10^{-6} \text{amp} \qquad (4\text{-}4)$$

At 300 μA (the maximum current in the exponential region of operation) the minimum number of lattice sites is 188. Using this value for N Eqn. (4-3) can be solved for the binding energy.

$$Q_o = 1.52 \text{ ev.} \qquad (4\text{-}5)$$

An approximate value for the radius at the tip of the liquid cone can be obtained by equating the coefficients of the arguments of the exponentials in Eqns. (4-1) and (4-2).

$$1.5 \times 10^{-3} \mathcal{E}^{1/2} = 0.75\ V^{1/2} \qquad (4\text{-}6)$$

In order to solve this equation, the relationship between the applied voltage and electric field at the tip of the liquid cone given by Eqn. (2-13) must be used. Eqn. (2-13) was derived for a system in which the cathode was an equipotential surface in the conical geometry. In the experimental geometry, the planer accelerating electrode does not possess the shape of an equipotential in conical geometry; therefore, the interelectrode spacing a_1, cannot be directly determined. Intuitively, one would surmise that the effect of the planer cathode and the cylindrical capillary would be to concentrate the field lines at the conical tip and thus enhance the field.

An approximate value for the electrode spacing can be obtained by determining the minimum applied voltage that is necessary to support the conical geometry. For the gallium-indium alloy the voltage is given in terms of the electrode spacing by(27)

$$V_0 = 3.58 \times 10^4 (a_1)^{1/2} \qquad (4\text{-}7)$$

The minimum voltage needed for the conical geometry was experimentally found to be 6.35 KV. This corresponds to an effective interelectrode spacing of approximately $a_1 = 0.031$ cm. whereas the actual geometric separation was 0.15 cm. Therefore, the distorted electrode geometry enhanced the field at the tip of the cone.

Using the above value for a_1, Eqn. (2-13) can be used to determine the electric field-voltage relationship at the tip of the cone. Further, by substituting Eqn. (2-13) into (4-6) the radius at the tip of the liquid cone was determined to be

$$\rho_o = 520\ \text{Å} \tag{4-8}$$

The upper and lower limits on the range of the emitted current were dictated by the corresponding ranges of the applied accelerating voltage. At capillary currents in the 20 to 50 microamp range the applied voltage was marginal with respect to support of the conical geometry. At these low current levels the meniscus would at times oscillate due to a Rayleigh-Taylor instability as given by Eqn. (1-21). The lowest unstable mode for a liquid hemisphere at a capillary tip is the n = 2 mode. For the Gallium-indium working fluid and a 125 μm radius capillary the unstable voltage is given by

$$V = (5\gamma\pi a\ (300)^2)^{1/2} = 6.5\ \text{KV} \tag{4-9}$$

This value of voltage for the n = 2 instability is within 3% of the 6.31 to 6.35 KV range of applied voltages needed to produce 20 - 50 microamps of emitted current. (See Fig. (4-3)).

In this mode of operation the emitted current was observed as a train of periodic pulses as shown in Fig. (4-4a) for a current of 20 μA. The expansion of a single pulse in Fig. (4-4b) shows that each pulse was actually composed of many charged particles. As the current level was changed the pulses remained nearly constant, but the frequency of the pulses varied. Photomicrographs of the liquid meniscus shown in Fig. (4-4c) depict the oscillatory motion of the n = 2 instability.

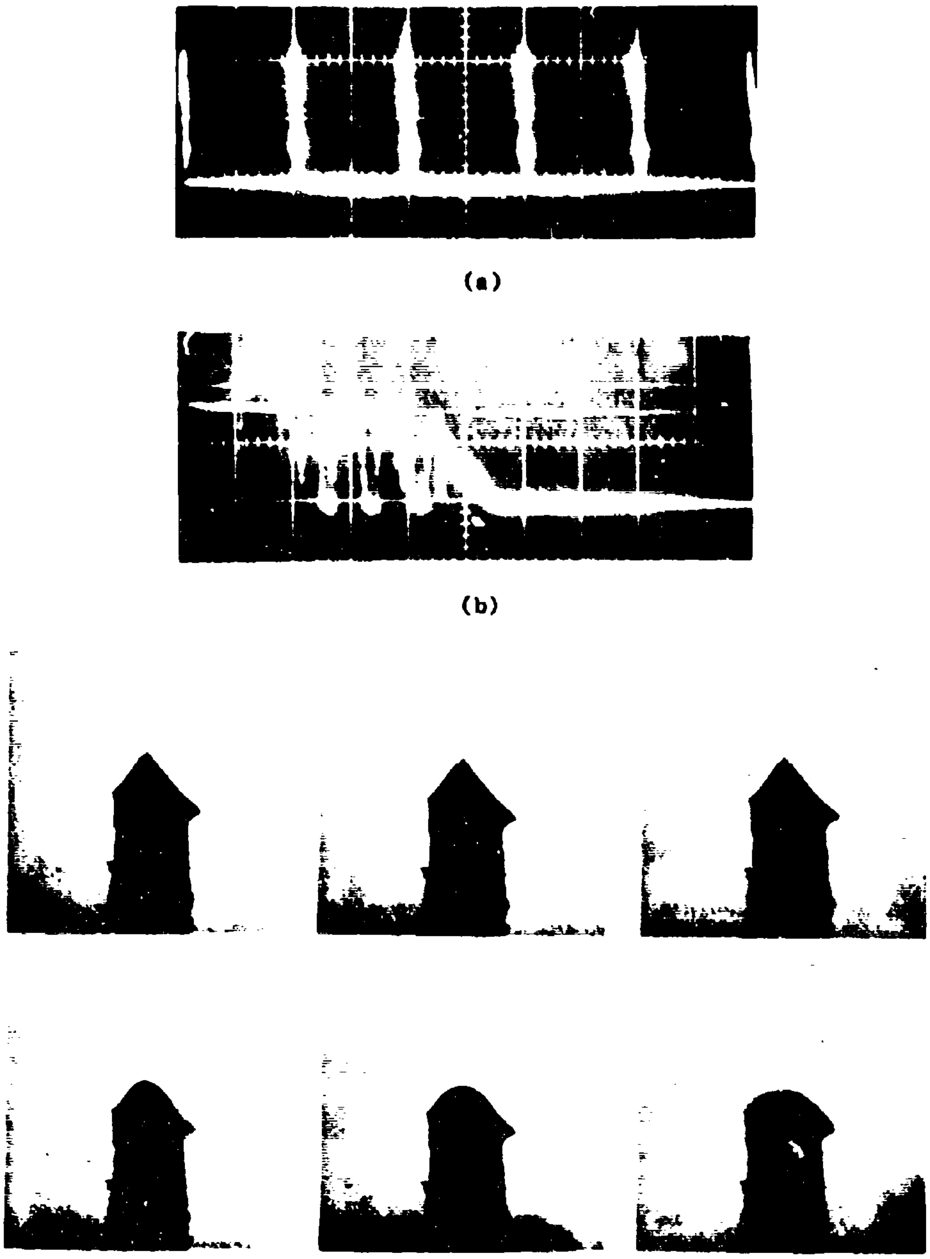

(a)

(b)

(c)

FIG. 4-4 LOW VOLTAGE INSTABILITY. (a) EMITTED CURRENT PULSES AT 1 ms/cm SWEEP SPEED. (b) SINGLE PULSE AT 20 μs/cm SWEEP SPEED. (c) PHOTO-MICROGRAPHS OF MENISCUS AT 20 μs INTERVALS.

At currents in excess of 500 microamps the second unstable Rayleigh-Taylor mode produced oscillations in the liquid cone. In the n = 2 mode, the liquid cone underwent longitudinal oscillations. For the second unstable mode, n = 3, the oscillations were in a transverse direction. In this mode the unstable applied voltage is given by

$$V = (7\gamma \pi a \; 9 \times 10^{4})^{1/2} = 7.7 \text{ KV} \qquad (4\text{-}10)$$

Experimentally this instability was detected at approximately 6.88 KV. The predicted unstable voltage is higher than the experimental value by 10%. This discrepancy can be explained by noting that in the derivation of Eqn. (1-21) the electric field normal to the meniscus was assumed to be equal to the field about a sphere. The effect of the conical shape would be to concentrate the field lines at the tip of the hemisphere and thus lower the unstable voltage. Photomicrographs of the n = 3 instability at a capillary current of 750 microamps are shown in Fig. (4-5).

4.3 Specific Charge Measurement

The specific charge distribution of the field evaporated particles was determined by use of both the time-of-flight mass spectrometer (TOFMS) and the quadrupole mass filter. Data points were obtained at 50 microamp intervals for capillary currents ranging from 50 to 500 microamps. Over this entire range of operating currents the specific charge distribution remained constant to within the accuracy of the detection apparatus, which was approximately 1% of the total detected current.

The quadrupole mass filter was used to obtain high resolution spectra of near axial particles and thus sampled only a very small portion of the

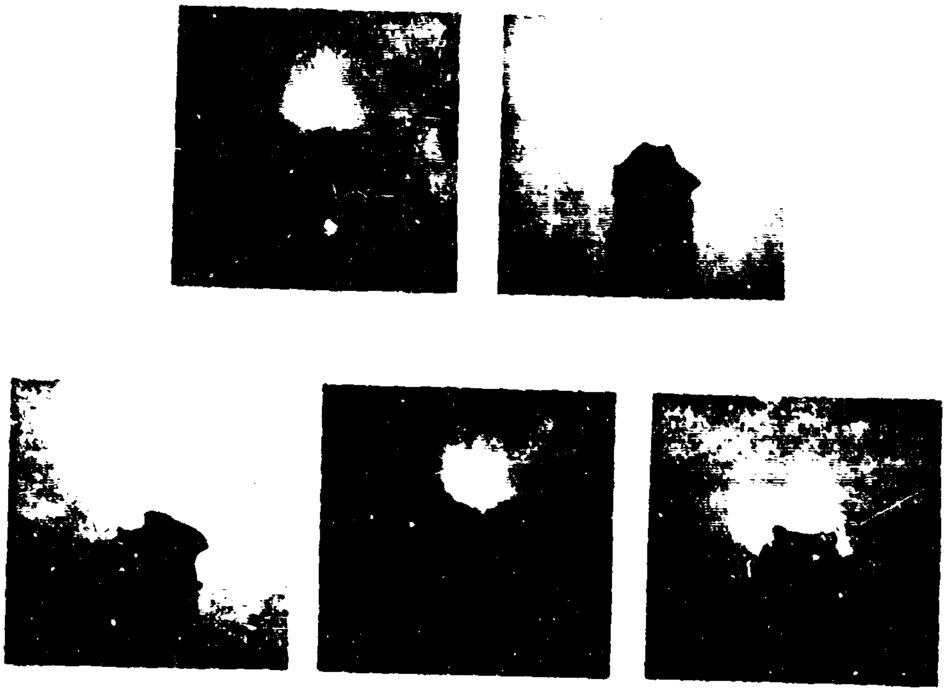

FIG. 4-4 PHOTOMICROGRAPHS OF HIGH VOLTAGE INSTABILITY

beam. A typical specific charge distribution is shown in Fig. (4-6). The spectrum was found to consist of 75% gallium dimers, 24% indium dimers and less than 1% gallium tetramers. The corresponding specific charges are shown in Table (4-1).

TABLE (4-1) SPECIFIC CHARGE DISTRIBUTION

Ionic Species	Percentage	Specific Charge
Ga_2^+	75	7.1×10^5 coul/kg
In_2^+	24	4.3×10^5 coul/kg
Ga_4^+	1	3.5×10^5 coul/kg

The specific charges of the field evaporated particles were all found to lie between $(3.5 - 7.1) \times 10^5$ coul/kg. The average specific charge of the beam was 6.3×10^5 coul/kg.

The quadrupole mass filter data was corroborated by the TOFMS. The TOF device was capable of detecting all particles spraying within a cone of 30° apex angle, but it was inherently a low resolution device. A typical TOF collector waveform is shown in Fig. (4-7a). By numerically differentiating this curve, the specific charge distribution is obtained as per Eqn. (3-11) and is plotted in Fig. (4-7b).

The TOF spectrum has broad peaks centered at 5.1×10^5 coul/kg and 8.1×10^5 coul/kg, with amplitudes of 22% and 78% of the total current respectively. The width of these peaks and their deviations from the quadrupole data can be explained by considering the basic limitations of the TOF measurement technique. First looking at Fig. (4-7a), the collector waveform is not rectangular (as it would be ideally), but it is rounded. This rounding tends to obscure the peaks of the spectrum and broaden them. It was caused by the finite rise time of the collector circuitry, and the

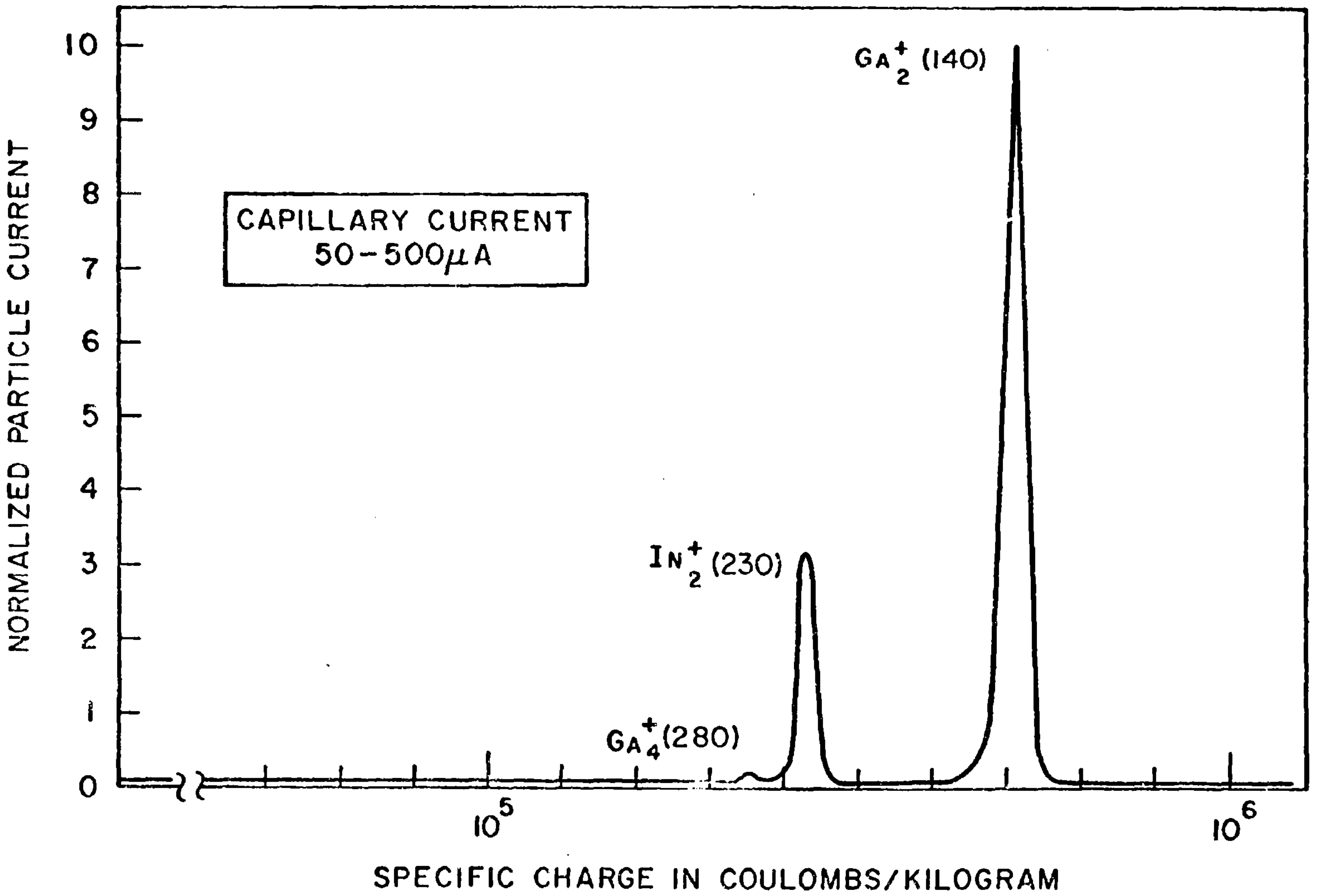

FIG. 4-6 SPECIFIC CHARGE DISTRIBUTION DETERMINED BY QUADRUPOLE MASS FILTER

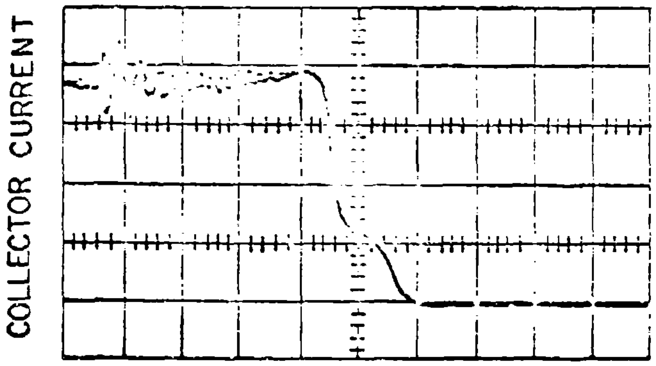

SWEEP SPEED = 0.5μ sec./cm

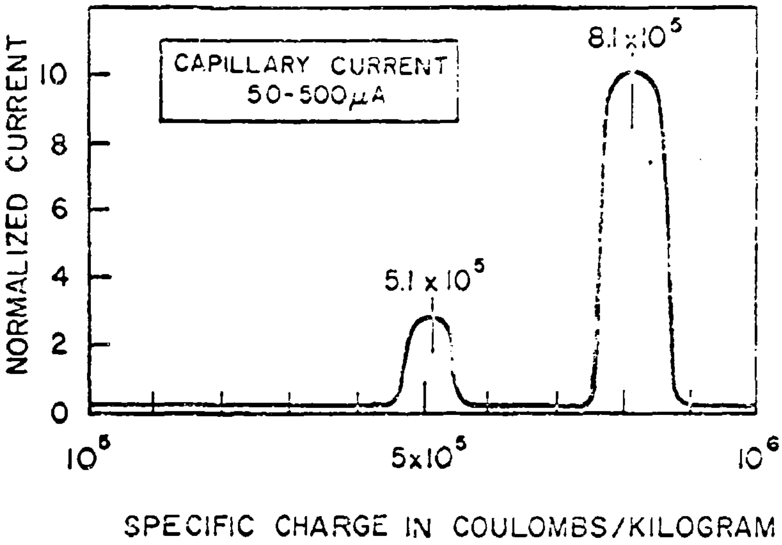

FIG. 4-7 TIME-OF-FLIGHT MASS SPECTROMETER CURRENT WAVEFORM AND SPECIFIC CHARGE DISTRIBUTION

high velocity of the emitted particles which necessitated a 0.5 microsecond/cm sweep speed. The resolution was further limited by the line width of the oscilloscope trace.

The second fundamental limitation is the establishment of a time base for the oscilloscope sweep relative to the high voltage pulse. It is necessary for the high voltage to start to decline in order to trigger the oscilloscope sweep. Thus the zero on the oscilloscope display corresponds to some positive instant in time relative to the high voltage pulse, and the entire waveform is shifted in time. A shift in the time scale of 200 nanoseconds would align the TOF spectra with the higher resolution quadrupole data.

The limitation in resolution is justified by the large cross-section of the beam that the TOFMS can detect. Since the composition of the working fluid is known, only gallium and indium ions can be present in the beam. Thus, the accuracy of the TOF technique is sufficient to determine the particular specific charges in the beam, and it can be assumed that the two TOF peaks correspond to gallium and indium dimers.

4.4 Formation Energy Measurement

The formation energy of the field evaporated ions was determined by utilizing the retarding potential cell. Data points were taken at 10 volt intervals in the retarding voltage while maintaining the accelerating voltage constant to within 10 volts. Data runs were made at 50, 100, 200, 300, 400, and 500 microamps capillary current. At all current levels the formation energy distribution was approximately gaussian. As the current was increased from 50 to 200 microamps, the position of the maximum and the variance of the distribution increased. In the 200 to 500 microamp range the energy distribution remained constant to within the 10 volt accuracy of the measurement technique.

The retarding potential current-voltage characteristics are shown in Fig. (4-8). By differentiating these curves the energy distributions are obtained and they are plotted in Fig. (4-9). The maximum of the energy distributions and the corresponding variances are listed in Table (4-2).

TABLE (4-2) FORMATION ENERGY DISTRIBUTION

Current	Peak Energy	Variance
50 μA	60 volts	$(38)^2$
100 μA	75 volts	$(42)^2$
200-500 μA	85 volts	$(47)^2$

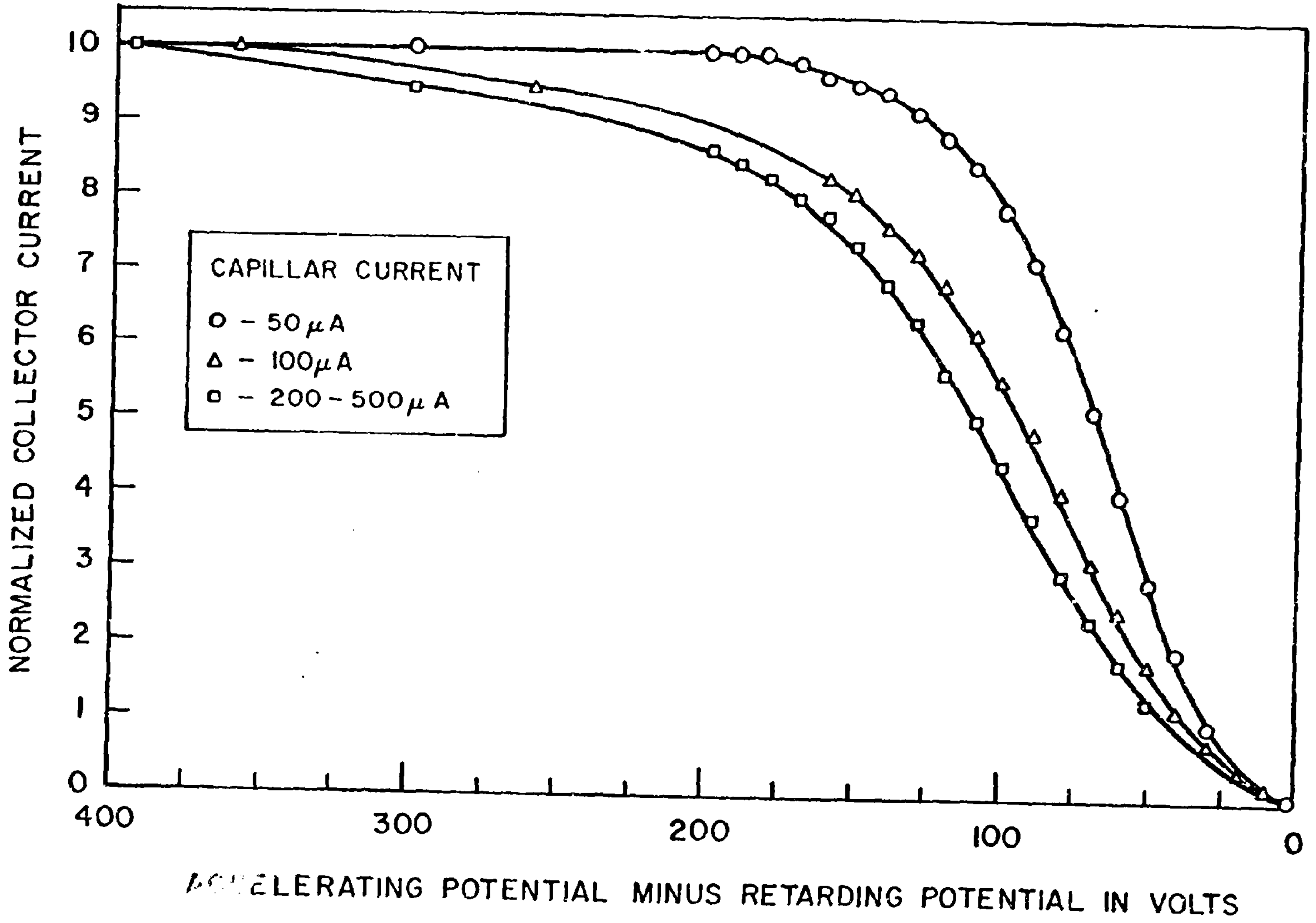

FIG. 4-8 RETARDING POTENTIAL CURRENT-VOLTAGE CHARACTERISTIC

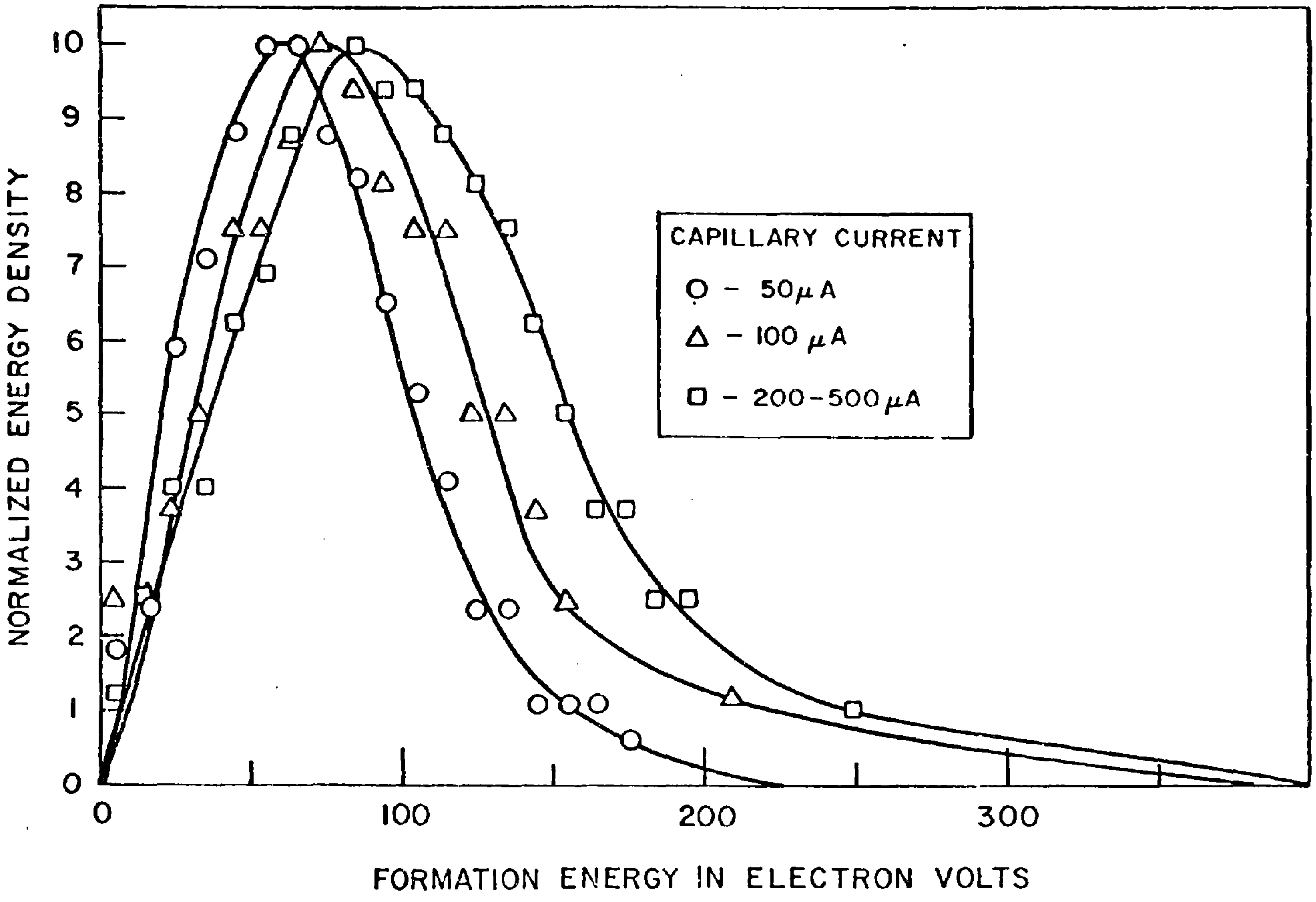

FIG. 4-9 ENERGY DISTRIBUTION OF FIELD EVAPORATED PARTICLES

5. CONCLUSIONS

This study has shown that under the appropriate operating conditions, EHD spraying techniques can be utilized for the production of high current density ion beams. The effects of capillary wetting and the feedback control (current regulation) of the accelerating voltage were responsible for the performance obtained. Without these techniques ions and heavy particles would have been simultaneously produced, and the present wide dynamic range of operation currents would not have been attained.

5.1 Comparison with Previous Results

Several close analogies can be drawn between the operation of an EHD spray operating in the field emission mode and the results of previous experiments utilizing an EHD spray for the production of heavy charged particles. The instabilities of the liquid meniscus during both low and high field operation correlate very closely with the extension of Rayleigh's theory derived by Hendricks(18) et al.. The close experimental agreement (3%) with theory for the minimum spraying potential for the $n = 2$ instability complements previous results using liquids with low conductivity. Hence, for a range of 15 orders of magnitude of conductivities, the modification of Rayleigh's theory applicable to a liquid hemisphere at the tip of an electrified capillary has been experimentally verified. Thus except for the number of unstable eigen-frequencies allowed, the behavior of an electrodynamically unstable liquid hemisphere appears to be physically the same as that of an electrodynamically unstable free charged sphere.

The operation of an EHD spray at voltages near the minimum spraying potential was previously observed by Carson.(36) The longitudinal oscillation of the liquid meniscus at low voltages corresponds to Carson's "naturally pulsed" mode of operation. Oscilloscope traces of the emitted current pulses have indicated that each pulse is actually composed of many charged particles. This result is also in agreement with Carson but contradicts Pierce's(37) theory that only one particle is produced per pulse. This may be the result of an inability to resolve the major current pulses into a fine structure which would support Pierce's contention.

The physical phenomenon responsible for the production of these pulsations has not been determined. Several possible mechanisms in low conductivity liquids (i.e. charge relaxation time and thermal effects) have been studied by Hendricks and Crowley.(38) The observed pulsations with the gallium-indium working fluid precludes the effects of electrical and thermal time constants in the liquid. It may be that the frequency of the observed pulses for high conductivity liquids is governed by the external time constant of the accelerating voltage supply.

Unlike the EHD spraying of low conductivity liquids where the charged particle beam has been assumed to be produced from an unstable meniscus, the emission of ions from the gallium-indium working fluid was by a direct interaction of the applied field on the surface without a bulk mechanical oscillation. Hence, a different functional relationship between the specific charge of the emitted particles and the applied field was obtained. Pfiefer's(19) energy minimization analysis of an unstable liquid plane predicts a specific charge varying as the one-half power of the applied field as shown in Eqn. (1-22). As the field intensity is increased the current is increased due to an increase in the specific charge of the emitted particles. In the field evaporation mode of spraying the specific charge of the emitted particles is constant, and the current is increased by increasing the number of particles produced per second.

5.2 Critique of Theoretical Considerations

In this section the models developed to explain the field evaporation mode of EHD spraying will be summarized. The predicted conical meniscus was observed for a wide range of applied electric field intensities. Taylor's theoretical apex angle of 98.6^{o} was observed along with angles ranging from 60^{o} to 110^{o}. In general the angle appeared to be determined by the mass of working fluid in the meniscus and not by the Taylor stability criteria. The present experiment differed from that assumed in Taylor's derivation in three important aspects: (1) The field about the cone was not uniform; (2) The meniscus was not a free surface but was constrained by the capillary; and (3) The internal pressure within the meniscus was non-zero. These three effects combined to allow the experimentally observed range of "stable" apex angles.

The experimental current-voltage relationship given in Eqn. (4-1) agrees with the functional dependence predicted by the field evaporation theory. The exponential nature of the I-V curve tends to make curve fitting very inaccurate; therefore, the experimental I-V curve in itself does not justify the use of the field evaporation model. Further evidence, however, supporting the field evaporation theory is gained from the specific charge distribution of the emitted particles and the electric field intensity at the conical surface. The ion-sized particles produced, the extremely high field intensities measured, and the experimental I-V curve all serve to indicate that a field evaporation phenomenon is responsible for the production of the high current density ion beam.

The electric field intensity at the apex of the meniscus can be calculated from Eqn. (2-13) by assuming the radius at the apex of the cone to be 520 Å as determined in Eqn. (4-8).

$$\mathcal{E} = 2.5 \times 10^5 \, V_0 \qquad (5\text{-}1)$$

The electric field intensity for a current of 300 μA is then 1.67×10^9 volts/meter.

Over forty elements have been field evaporated.(30) In Fig. (5-1), the evaporating field strengths of a representative group of these elements are plotted as a function of their binding energies. The present data for the gallium-indium working fluid is included using the experimentally determined values for the electric field intensity and binding energy.

The only significant loss mechanism in the ion beam formation was through the space charge of the emitted particles. Losses due to both the binding energy of the atoms and the finite conductivity of the working fluid were found to be negligible in comparison to the kinetic energy of the ions. The predicted potential loss due to the space charge, as given by Eqn. (2-38) and the peak values of the experimental retarding potential curves are listed in Table (5-1) as a function of the emitted current.

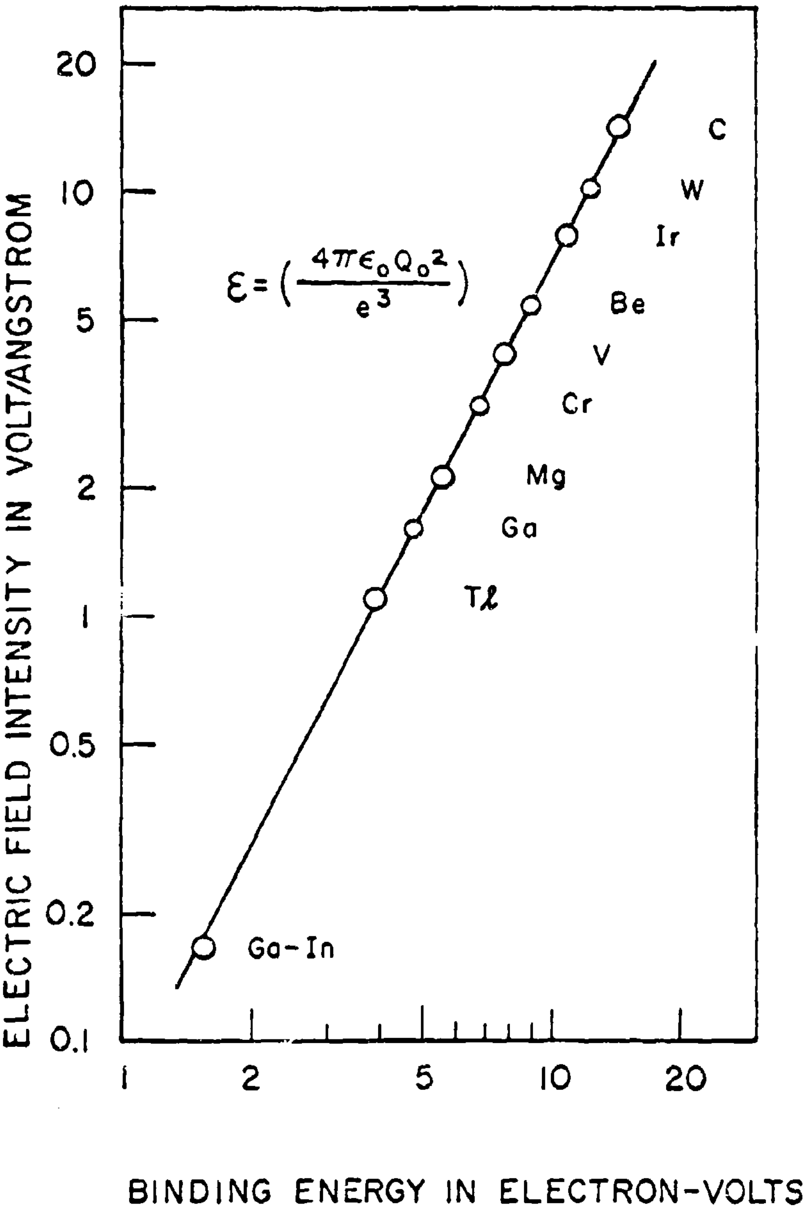

FIG. 5-1 EVAPORATING ELECTRIC FIELD INTENSITY AS A FUNCTION OF BINDING ENERGY

TABLE (5-1) THEORETICAL AND EXPERIMENTAL FORMATION POTENTIALS

I (μA)	Theoretical Potantial (V)	Experimental Potential (V)
50	16	60
100	31	75
200	62	85
300	92	85
400	121	85
500	151	85

The poor agreement between the theoretical and experimental data indicates that the proposed space charge model is at best a poor approximation to the actual physical phenomenon. The basic assumptions in the derivation of Eqn. (2-38) of a constant current density and a parallel ion beam were violated by the experimental system where, in essence, the beam was diverging from a near point source. Also, the total emitted current and the current density were not linearly related. As the current was increased the emitting area also increased.

5.3 Thruster Utilization

The usefulness of the field evaporated dimer beam as a microthruster can be determined by considering the following parameters: (1) Thrust; (2) Particle formation efficiency; and (3) Beam conversion efficiency.

An electrostatically accelerated beam of gallium and indium dimers produces a thrust given by Eqn. (1-4).

$$F = 1.78 \times 10^{-3}\, I V_a^{1/2} \tag{5-2}$$

The 20 - 500 microamp range of emitted currents that can be produced leads to a range of thrusts varying from 2.8 to 73.8 micronewtons (1.3 to 33.5 micropounds). The thrust is listed as a function of the current and accelerating voltage in Table (5-2).

TABLE (5-2) THRUST AS A FUNCTION OF CURRENT AND ACCELERATING VOLTAGE

I (μA)	V (kv)	F (μN)
20	6.31	2.8
50	6.35	7.1
100	6.44	14.4
200	6.57	28.9
300	6.68	43.6
400	6.78	58.6
500	6.88	73.8

As the thrust is increased the accelerating voltage remains nearly constant; therefore, the velocity of the emitted particles remains essentially constant, and they could be maintained at a near optimum velocity independent of the thrust level.

The particle formation efficiency of the charged particle beam can by computed by substituting the retarding potential data into Eqn. (1-5). The formation efficiency is listed as a function of the emitted current in Table (5-3).

TABLE (5-3) FORMATION EFFICIENCY AS A FUNCTION OF EMITTED CURRENT

I (μA)	η_f (%)
50	99.1
100	98.8
200	98.7
300	98.8
400	98.8
500	98.9

The approximately 1% loss in efficiency was previously attributed to space charge effects. This energy loss appears as a transverse acceleration of the ions and leads to beam spreading. Such a divergent beam has reduced thrust producing capabilities compared to a parallel beam. It should also be noted here that all of the ions were not emitted with parallel trajectories. In addition to the losses given above there was an inherent beam spreading due to the electric field geometry at the capillary tip.

The constant specific charge distribution of the particles produced by the field evaporation process leads to a constant beam conversion efficiency independent of the thrust level. By substituting the experimentally determined specific charge distribution into Eqn. (1-12), the beam conversion efficiency was found to be

$$\eta_b = 97.5\% \tag{5-3}$$

Thus, the distribution of specific charges present in the beam degrades the thrust producing capability of the system by 2.5%.

In summary, the ion beam produced by EHD spraying techniques has been shown to be useful as a source of ionic particles for micro-thruster utilization. The high thrust produced, high formation efficiency, and high beam conversion efficiency lead to a system combining the advantages of existing ionic and heavy particle electrostatic thrusters.

5.4 Recommendations for Future Research

The present solutions to the problems encountered in the course of this study have left many questions unanswered and have produced many more new areas of interest for future research. Some of the more pertinent problems are described below.

(1) Apply feedback control (current regulation) to the EHD spraying of various working fluids. Construct conical electrodes so that a uniform field is obtained and Taylor's stability theory can be verified. Analyze the parameters of the sprayed particles as a function of liquid conductivity, surface tension and viscosity.

(2) Obtain a solution of Child's law for the conical electrode configuration so that a precise analysis of space charge effects may be carried out.

(3) Extend Taylor's conical stability criterion from the free surface case to the case of a liquid meniscus constrained by a capillary.

(4) Using the present experimental geometry, study the field evaporation of other conducting liquids such as mercury, cesium, sodium, and potassium to determine their usefulness in electrostatic thrusters.

(5) Spray pure gallium instead of the alloy and determine the effect of temperature on the field evaporation process.

(6) Explore the possibility of producing higher currents and thrusts by utilizing a different source geometry such as an annulus, thin slit,

or rotating disc.

(7) The addition of an AC component at an unstable Rayleigh eigenfrequency to the accelerating voltage could enhance the breakup of the meniscus into larger particles. Such particles could be useful in heavy particle propulsion systems.

(8) Study post acceleration or deceleration of the field evaporated ions as a means of obtaining an optimum exhaust velocity.

(9) Determine the effects of intense negative fields on liquid metals. Preliminary studies produced a 10 mA electron source from a single capillary.

(10) Analyze the effect of the accelerating voltage supply impedance on the "naturally pulsed" mode of EHD spraying for both conducting and non-conducting liquids.

(11) Study the systems aspects of microthrusters. Construct a working thruster module composed of an array of capillaries operating in the field evaporation mode capable of producing 0.5 millipounds of thrust.(39) Perform 10,000 hour life tests to determine reliability for space applications. Analyze the compatibility of above system with respect to thrust vectoring, propellant feed systems, and power conditioning of the output from present photovoltatic sources.

LITERATURE CITED

1. Tsiolkovskii, K.E.: Collected Works, Izd. Akad. Nauk. SSSR Moscow, Tompervyi, Aerodynamics, Vol. 1, p. 266, 1951.

2. Goddard, R.H.: "R.H. Goddard: an Autobiography," Astronautics, Vol. 4, p. 24, 1959.

3. Stuhlinger, E.: Ion Propulsion for Space Flight, McGraw Hill, New York, 1964.

4. Rutherford, E.: "The Velocity and Rate of Recombination of the Ions of Gases Exposed to Roentgen Radiation," Phil. Mag. Ser. 5, Vol. 44, p. 422, 1897.

5. Thomson, J.J.: "Conduction of Electricity Through Gases," Cambridge University Press, New York, 1903.

6. Langmiur, I., and K.H. Kingdon: "Thermionic Phenomena Due to Alkali Vapors," Phys. Rev., Vol. 21, p. 380, 1923.

7. Taylor, J.B., and I. Langmiur: "The Evaporation of Atoms, Ions, and Electrons from Cesium Films on Tungsten," Phys. Rev., Vol. 44, p. 423, 1933.

8. Finkelstein, A.T.: "A High-Efficiency Ion Source," Rev. Sci. Instr., Vol. 11, p. 94, 1940.

9. Ardenne, M. von: "New Developments in Applied Ion and Nuclear Physics," At. Energy Res. Estab. Gt. Brit. Lib. Trans. 758, Harwell, Berkshire, England, 1957.

10. Stuhlinger, E.: "Possibilities of Electrical Space Ship Propulsion," Proc. 5th Intern. Astronaut. Federation Congr. Innsbruck, p. 100, 1954.

11. Cho, A.Y. and C.D. Hendricks: "Analytical and Experimental Study of Porous Metal Ionizers," Final Report NASA Contract NAS-3-8904, Charged Particle Research Laboratory, University of Illinois, 1967.

12. Bose, G.M.: "Recherches Sur La Cause et Sur La Véritable Théorie de L'Electricité," Wittenberg, 1745.

13. Lord Rayleigh: "On the Equilibrium of Liquid Conducting Masses Charged with Electricity," Phil. Mag. Series 5, Vol. 14, p. 184, 1882.

14. Drozin, V.: "The Electrical Dispersion of Liquids as Aerosols," J. Colloid Sci., Vol, 10, p. 158, 1955.

15. Hendricks, C.D.: "Charged Droplet Experiments," Proceedings of the Second Symposium on Advanced Propulsion Concepts, Oct. 1959, Boston, Mass., See also J. Colloid Sci., Vol. 17, p. 249, 1962.

16. Hendricks, C.D.: "Charged Heavy Particles for Propulsion Systems," Second Quarterly Report, Contract No. C93A-1009, Charged Particle Research Lab., University of Illinois, Urbana, Illinois 1960.

17. Krohn, V.E.: in Progress in Astronautics and Rocketry, D.B. Langmiur, E. Stuhlinger, and J.M. Sellen, Jr., Eds. Vol. 5, p. 73, Academic Press Inc., New York, 1961.

18. Hendricks, C.D., R.S. Carson, J.J. Hogan and J.M. Schneider, "Photomicrography of Electrically Sprayed Heavy Particles," AIAA Journal, Vol. 2, No. 4, p. 733, 1964.

19. Pfeifer, R.J.: "Parametric Studies of Electrohydrodynamic Spraying," Ph. D. Dissertation, Elec. Eng. Dept. University of Illinois, 1965.

20. Müller, E.W.: "Field Desorption," Phys. Rev., Vol. 102, p. 620, 1956.

21. Müller, E.W.: "Field Ionization and Field Ion Microscopy," in Advances in Electronics and Electron Physics, Vol. XIII, p. 83, Academic Press, New York, 1960.

22. Müller, E.W., and K Bahadur: "Field Ionization of Gases at a Metal Surface and the Resolution of the Field Ion Microscope," Phys, Rev., Vol. 102, p. 624, 1956.

23. Swatik, D.S.: "Electrohydrodynamic Spraying of Gallium-Indium Alloy," Master's Thesis, Elec. Eng. Dept. University of Illinois, 1967.

24. Hamilton, J.H., J.R. Lewis and J.P. Denny. "Physical Chemistry of Gallium-Indium Alloys," Project NR-052-109, Utah Eng. Exp. Station, University of Utah, 1950.

25. Roseburg, F.: Handbook of Electron Tube and Vacuum Techniques, Addison-Wesley, Reading, Mass., 1965.

26. Zrnic, D. and D.S. Swatik: "On the Resistivity and Surface Tension of the Eutectic Alloy of Gallium and Indium," Journal of Less-Common Metals, Vol. 18, pp. 67-68, 1969.

27. Taylor, G.: "Disintegration of Water Drops in an Electric Field," Proceedings of the Royal Society (London), Series A, Vol. 280, No. 1382, pp. 383-397, 1964.

28. Gomer, R.: "Field Desorption," Journal Chem. Phys. Vol. 31, p. 341, 1959.

29. Gomer, R. and L.W. Swanson: "Theory of Field Desorption," Journal Chem. Phys, Vol. 38, p. 1631, 1963.

30. Brandon, D.G.: "Field Evaporation," in Field Ion Microscopy, edited by J.J. Hren and S. Ranganathan, Plenum Press, 1968.

31. Samsonov, G.V. editor. Handbook of the Physicochemical Properties of the Elements, IFI/Plenum, New York, 1968.

32. Wilson, A.B.: Personal Communication, Special Processes Lab., Dept. of Elec. Eng. University of Illinois, 1968.

33. Harmon, W.W.: Fundamentals of Electronic Motion, McGraw-Hill, New York, 1953.

34. Pichanick, F.M.J.: "The Use of Quadrupole Fields," in Methods of Experimental Physics, edited by L. Marton, Vol. 4, Part A, Academic Press, New York, 1967.

35. Pfeifer, R.J. and C.D. Hendricks: "Parametric Studies of Electrohydrodynamic Spraying," AIAA Journal, Vol. 6, No. 3, pp. 496-502, 1968.

36. Carson, R.S. and C.D. Hendricks: "Natural Pulsations in Electrical Spraying of Liquids," AIAA Journal, Vol. 3, No. 6, p. 1072, 1965.

37. Pierce, E.T.: "Effects of High Electric Fields on Dielectric Liquids," JAP, Vol. 30, p. 445, 1959.

38. Hendricks, C.D., and J.M. Crowley: "Electrohydrodynamic Processes in Electric Field Spraying of Liquids," Paper presented at International Symposium on Electrohydrodynamics, MIT, 1969.

39. Atkins, K.: "A General Method for Comparing Advanced Low Thrust Space Propulsion Devices," Ph. D. Dissertation, To be submitted to Elec. Eng. Dept. University of Illinois, 1969.